Journal of the Meteorological Society of Japan

EARLY ONLINE RELEASE

The DOI for this manuscript is

DOI:10.2151/jmsj.2020-052

J-STAGE Advance published date: July 9th 2020

A comparison of the effects of an upper-level anticyclone and a lower-level cyclone on tropical cyclogenesis in idealized simulations

Xi Cao[1, 2, 3]*, Renguang Wu[4, 1], Yifeng Dai[5] and Jing Xu[2]

[1]*Center for Monsoon System Research, Institute of Atmospheric Physics, Chinese Academy of Sciences, Beijing, China*

[2]*State Key Laboratory of Severe Weather, Chinese Academy of Meteorological Sciences, Beijing, China*

[3]*Shanghai Typhoon Institute, China Meteorological Administration*

[4]*School of Earth Sciences, Zhejiang University, Hangzhou, Zhejiang, China*

[5]*Tongji Zhejiang College, Jiaxing, Zhejiang, China*

Journal of the Meteorological Society of Japan

Submitted on 28 October, 2019

Revised on 29 January, 2020

Revised on 7 April, 2020

Revised 11 May, 2020

Revised 8 June, 2020

Corresponding author:

Dr. Xi Cao. Building 40, Huayanli, Beichen West Road, Chaoyang District, Beijing 100029, China. Email: caoxi09@mail.iap.ac.cn

Abstract

The effects of an upper-level anticyclonic circulation and a lower-level cyclonic circulation on tropical cyclone (TC) genesis are examined by idealized simulations using the Advanced Research Weather Research and Forecasting (WRF-ARW) model. The simulation results show that the upper-level anticyclonic circulation makes a negative contribution to TC genesis, whereas the lower-level cyclonic circulation makes a positive contribution. The upper-level anticyclonic circulation results in slower TC genesis due to a large vertical zonal wind shear that shifts the upper-level vortex eastward from its initial position, which is unfavorable for the vertical alignment and warm core maintenance of the vortex. This large vertical zonal wind shear is associated with the asymmetries of the vertical motion and associated diabatic heating induced by the lower-level beta gyre. The upper-level anticyclonic circulation increases the westerly wind to the north of the vortex, resulting in a large vertical westerly wind shear. Thus, the initial upper-level anticyclonic circulation is not necessary for TC genesis, and the strong upper-level anticyclonic circulation generally observed with a strong TC should be regarded as a result of deep convection. In contrast, strong lower-level winds due to the superposition of the large-scale lower-level cyclonic circulation and vortex induce large surface heat fluxes and vorticity, leading to strengthened convection and diabatic heating and a quick build-up of positive vorticity, resulting in rapid TC genesis.

Key words: Upper-level anticyclonic circulation; lower-level cyclonic circulation; idealized simulation; tropical cyclone genesis

1. Introduction

Tropical cyclone (TC) genesis is characterized by the transformation of a random cumulus-scale convective system into a self-sustaining synoptic-scale cyclonic system with a warm core under favorable large-scale conditions. How a weak tropical disturbance intensifies within a synoptic-scale environment has intrigued researchers for decades. Some observational studies have focused on how the upper-level circulation affects TC intensification. Merrill (1988) suggested that when one or two outflow channels exist at the upper level, TCs intensify at a quick rate during the Atlantic storm season, while TCs generally intensify at a slow rate when there is a closed circulation without an outflow channel because TCs are unable to ventilate mass in the outflow layer. On the other hand, the intensification of TCs can also be linked to the establishment of a tropical upper tropospheric trough, which is favorable for vigorous convection in the inner core (Sadler, 1976; Holland and Merrill, 1984).

In addition to external environments at the upper level, Wang (1998, hereafter W98) studied the influence of the vertical structure of a vortex on TC intensification using an idealized model. W98 suggested that a vortex having a maximum tangential wind of 30 m s^{-1} without an upper-level anticyclone can intensify at a more rapid rate than a vortex with an upper-level anticyclone. However, there is a lack of detailed analyses on the relative importance of an upper-level anticyclonic circulation and a lower-level cyclonic circulation in TC genesis. Although TCs have received much attention regarding the relationship between upper-level circulation and TC intensification in both observational and numerical studies (Holland and Merrill, 1984; DeMaria et al., 1993; Rappin et al., 2011; Leroux et al., 2013), relatively little research has been conducted on the relationship between upper-level conditions and TC genesis.

In an observational study, McBride and Zehr (1981, hereafter MZ81) found that developing cloud clusters generally exhibit enhanced lower-level positive vorticity, near-zero vertical wind shear over the vortex center, vertical westerly wind shear to the north and vertical easterly wind shear to the south. This vertical zonal wind shear pattern implies that a large-scale upper-level anticyclonic circulation and a large-scale lower-level cyclonic circulation are both favorable for TC genesis (Gray, 1968, 1998). However, another possible hypothesis is that a compensating upper-level anticyclonic circulation must develop due to the convergence of moisture and release of latent heat by deep convection,. Therefore, further investigation is desired to understand whether an upper-level anticyclonic circulation is necessary for TC genesis.

In addition to the role played by the upper-level anticyclonic circulation, most observational studies have indicated that the lower-level circulation plays an important role in TC genesis (Gray, 1968; MZ81; Ritchie and Holland, 1999; Lee et al., 2008; Wu et al., 2013; Feng et al., 2014; Cao et al. 2016; Cao and Wu 2018a, 2018b; Cao et al. 2018, 2020). For example, Ritchie and Holland (1999) identified several typical circulation patterns, including monsoon shear lines, monsoon confluence zones, and monsoon gyres, associated with TC formation over the western North Pacific (WNP). Wu et al. (2013) examined monsoon gyre activity, structures, and the associated formation of TCs using 11-year reanalysis data. The identified 31 monsoon gyres were accompanied by the formation of 43 TCs, accounting for 20.3% of the total number of TCs during the TC season over the WNP. The recent modeling studies of Cao et al. (2014a, hereafter C14; 2014b) demonstrated that the intraseasonal oscillation and interannual variation of the monsoon trough exert strong controls on TC formation through both dynamic (vorticity and convergence) and thermodynamic (moisture) effects over the WNP. Although most of these studies were based on observations, it is unclear whether TC genesis facilitated by the lower-level circulation can be confirmed through idealized simulations in a full-physics model. Recently, some studies (Xu et al. 2016; Yan et al. 2019) found that a TC does not experience rapid formation and intensification when the TC is embedded within a monsoon gyre, which contradicts the observational studies.

Based on previous studies, the following intriguing questions can be raised: Are the upper-level anticyclonic circulation and lower-level cyclonic circulation equally favorable for TC genesis? How do the upper-level anticyclonic circulation and the lower-level cyclonic circulation play a role in TC genesis? This work attempts to address the aforementioned questions through a series of idealized simulations using a mesoscale model.

The remainder of this paper is organized as follows. The model and experimental design are illustrated in section 2. Section 3 describes the time evolutions of vortices, examines the mechanisms by which the upper-level anticyclonic circulation and lower-level cyclonic circulation impact TC formation, and discusses the sensitivity of vortex development to different structures of the upper-level anticyclonic circulation and initial conditions with lower-level cyclonic circulation included in additional experiments. Finally, a summary and a short discussion are given in section 4.

2. Model and experimental designs

2.1 Model

The results presented in this study are based on three idealized numerical experiments performed using the nonhydrostatic Advanced Research Weather Research and Forecasting (WRF-ARW; Skamarock et al., 2008) model (version 3.3.1). The model is triply nested with two-way interaction and fixed inner domains. The mesh sizes in the three domains are 241×241, 241×241, and 481×481 with horizontal grid sizes of 27, 9, and 3 km, respectively. There are 35 levels in the vertical direction from the surface to 10 hPa. The Kain–Fritch convective scheme is applied to the two outer meshes (Kain and Fritsch, 1993), and an explicit microphysics scheme (Lin et al., 1983) is used in all meshes. The model experiments are integrated to 120 h. The model is set on a beta plane at 15 °N. In the control experiment, the background environmental flow is quiescent and a constant sea surface temperature (SST) of 29 °C is specified. The environmental relative humidity and other thermodynamic variables are horizontally homogeneous based on January mean observations at Willis Island (Holland, 1997). The other modeling settings are identical to those illustrated in C14.

2.2 Experimental designs

The experiments are initialized with the same axisymmetric weak vortex. The maximum tangential wind of the vortex is 8 m s^{-1} at a radius of 150 km at the surface with the vertical profile of a sine function using the sigma vertical coordinate (Wang, 1995). In addition, an axisymmetric upper-level anticyclonic circulation and a lower-level cyclonic circulation are inserted into the background fields to examine the impacts of large-scale circulation on vortex development. The initial maximum tangential winds of the upper- and lower-level circulations are both 8 m s^{-1} at a radius of 700 km from the circulation centers, and both circulations have a vertical profile following a sine function. The upper-level anticyclonic circulation reaches its maximum intensity at 150 hPa; then, the intensity decreases both upward to zero at 100 hPa and downward to zero at 300 hPa. In contrast, the lower-level cyclonic circulation has a maximum intensity at the sea surface and gradually decreases upward to zero at 300 hPa. Given the wind fields, the mass and thermodynamic fields are derived based on a nonlinear balance equation so that the initial vortex, upper-level anticyclonic circulation, and lower-level cyclonic circulation all satisfy the hydrostatic and gradient wind balances (Wang, 1995). Note that there is no appreciable difference in the initial relative humidity around the cores of the vortices as a result of the balancing procedure (figure not shown). The upper-level anticyclonic circulation and lower-level cyclonic circulation are the background fields for the development of the initial vortex, not the vertical structure of the vortex.

The horizontal structure of the lower-level cyclonic circulation is similar to the lower-level component of a composite monsoon gyre (Wu et al., 2013). Note that the lower-level cyclonic circulation is not called a monsoon gyre because a typical monsoon gyre has a baroclinic vertical structure, which includes both the lower-level and the upper-level circulations (Wu et al., 2013; Yan et al., 2019). Furthermore, according to reanalysis data (see Fig. 2 of C14), the vertical structures of the upper-level anticyclonic circulation and lower-level cyclonic circulation are basically consistent with the vertical structure of the tangential wind during the active phase of the intraseasonal oscillation of the monsoon trough over the WNP. The tangential wind during the active phase of the monsoon trough intraseasonal oscillation is characterized by a typical baroclinic structure, which consists of an upper-level anticyclonic circulation above 300 hPa and a lower-level cyclonic circulation below 300 hPa.

The effects of the upper-level anticyclonic circulation and lower-level cyclonic circulation on TC genesis are studied by performing four experiments and comparing their results. In the control experiment (hereafter CTL), an initial weak vortex is placed in a resting environment. In one sensitivity experiment (hereafter SUA), the upper-level anticyclonic circulation is added to CTL as the background field of vortex development. In the second sensitivity experiment (hereafter SLC), we conduct the simulation in the same way except the lower-level cyclonic circulation is added to CTL. In the third sensitivity experiment (hereafter SUALC), we include both the upper-level anticyclonic circulation and the lower-level cyclonic circulation. In addition, to examine the potential influences of different structures of the upper-level anticyclonic circulation on TC genesis, four additional experiments are performed for further comparison; these additional experiments involve the modification of three parameters, namely, the height of the maximum upper-level anticyclonic circulation, the radius of the maximum anticyclonic wind, and the magnitude of the maximum anticyclonic wind. The details of the model experiments are provided in Table 1.

Figure 1 shows the initial wind fields at 150 hPa and 850 hPa and the vertical-radial cross section of the tangential wind of the vortex in the CTL, SUA and SLC experiments. It is obvious that the upper-level anticyclone is stronger in SUA than in CTL and SLC (Figs. 1a-c) and that the lower-level cyclone is stronger in SLC than in CTL and SUA (Figs. 1d-f). Furthermore, the tangential wind at the surface of vortex is greater outside of the maximum wind radius in SLC than in CTL and SUA (Figs. 1g-i).

3. Mechanism of impacts

3.1. Evolutions of the vortices

Figure 2 shows the time evolutions of the minimum sea level pressure (MSLP) and maximum azimuthal-mean wind (MAMW) at a height of 10 m in CTL, SUA, SLC, and SUALC from the 3-km simulation data. The vortices in the first 60 h experience adjustment and spin-up processes with little development and are followed by different intensification rates among the four cases. The development of vortices varies with the existing background flows on a beta plane. A strong TC develops at t = 120 h in SLC with an MSLP of 959 hPa, whereas the vortex develops much more slowly throughout the whole 120-h simulation in SUA with an MSLP of 994 hPa. The vortices in CTL and SUALC develop at rates between those in SLC and SUA with final MSLPs of 980 hPa and 967 hPa, respectively. The time when the MAMW at 10 m exceeds 15 m

s^{-1} is defined as the time of cyclogenesis. This definition may correspond to a peak wind in excess of 17 m s^{-1}, but denotes a relatively stable vortex. Based on this definition, tropical cyclogenesis occurs at t = 99 h in CTL and SUALC, at t = 117 h in SUA, and at t = 93 h in SLC.

In addition, the simulated TCs have a vertical structure typical of a strong TC at the end of the simulation. Figure 3 displays the vertical-radial cross sections of the azimuthal-mean tangential wind, radial wind, and diabatic heating fields in CTL, SUA, and SLC. The TCs in these three experiments are all characterized by a tilted eyewall and a salient "in–up–out" secondary circulation. In SLC, the maximum tangential wind reaches 58 m s^{-1} at a radius of nearly 40 km at 850 hPa (Fig. 3c). Furthermore, strong radial inflow and outflow layers occur in the planetary boundary layer (PBL) and upper level, respectively (Fig. 3f). The structures of the axisymmetric TC wind and heating fields in CTL and SUA are similar to those in SLC but with apparently weak magnitudes (Figs. 3a-b and Figs. 3d-e).

The modeling results indicate that the vortex with the enhanced lower-level cyclonic circulation has a rapid intensification rate, which is partly consistent with previous observational and numerical analyses insomuch that a preexisting weak disturbance in an environment with enhanced lower-level cyclonic vorticity is more likely to evolve into a TC (Gray, 1968, 1998; Zehr, 1992; Cao et al., 2012, 2014a, 2014b; Fu et al., 2012). However, Xu et al. (2016) showed that a vortex does not always experience rapid development when it interacts with a monsoon gyre. The discrepancy between the findings of this study and Xu et al. (2016) will be further discussed in the following section.

On the other hand, it is worth noting that the upper-level anticyclonic circulation makes a negative contribution to the development of the vortex compared to CTL. This result is inconsistent with the earlier study of MZ81, which reported that the presence of an upper-level anticyclonic circulation is necessary and favorable for TC genesis. However, our finding is consistent with the argument in W98 that during the intensification stage of vortex, a vortex without an upper-level anticyclonic circulation develops more quickly than a vortex with an upper-level anticyclonic circulation. We will further investigate why the upper-level anticyclonic circulation and lower-level cyclonic circulation have opposite effects on TC genesis in the following analyses.

3.2. Upper-level anticyclonic circulation

Figure 4 shows the evolutions of the wind field and zonal wind at 150 hPa in CTL, SUA, and SLC from the 27-km simulation data at t = 0 h, 72 h, and 120 h. At the initial time, the winds at 150 hPa in CTL and SLC are negligible, whereas a strong anticyclonic circulation appears in SUA (Figs. 4a, 4d, 4g). At t = 72 h, westerly winds almost prevail at the upper level in CTL and SUA, with the stronger winds appearing north of the vortex center in the latter (Figs. 4b, 4e). This result implies that obvious westerly winds are present in the upper level in SUA induced by the background large-scale circulation, resulting in a large vertical wind shear. In contrast, a relatively clear anticyclonic circulation develops, with weak easterly winds located on the southwest side of the vortex center in SLC (Fig. 4h). Toward the end of the simulation, the westerly winds on the north side of the vortex center intensify from 6 m s^{-1} to 14 m s^{-1} in CTL (Figs. 4b, 4c) and from 10 m s^{-1} to 14 m s^{-1} in SUA (Figs. 4e, 4f). Furthermore, there is obvious divergence around the vortex center, with easterly winds to the west and westerly winds to the east in CTL (Fig. 4c), while strong westerly winds are still dominant to the northeast in SUA (Fig. 4f). In the presence of the lower-level cyclonic circulation, a rather strong and organized anticyclonic circulation appears in SLC (Fig. 4i), implying that the upper-level anticyclonic circulation develops well due to well-organized deep convection.

In addition to the upper-level winds, we also examine the winds at the lower level (Fig. 5). Initially, the winds of the vortices are the same in CTL and SUA at 850 hPa (Figs. 5a, 5d), whereas the winds in SLC spread widely over a large area (Fig. 5g). At t = 72 h, although the extents of the vortices in CTL and SUA are almost the same, the wind magnitude is slightly larger in CTL than in SUA; this indicates that the upper-level anticyclonic circulation has an overall negative effect on vortex development (Figs. 5b, 5e). On the other hand, the wind magnitudes are almost the same in CTL and SLC with a maximum easterly wind of 10 m s^{-1} (Figs. 5b, 5h). However, the extents of the easterly and westerly winds are evidently broader in SLC than in CTL and SUA. At t = 120 h, the winds are much stronger in SLC than in CTL and SUA (Figs. 5c, 5f, 5i).

Based on the upper-level wind distributions in Fig. 4, Fig. 6 further shows the area-averaged (720 km × 720 km) vertical zonal wind shear, which dominates the total vertical wind shear, around the TC center between 150 hPa and 850 hPa from t = 0 h to t = 96 h. Note that 200 hPa and 850 hPa are conventional choices for calculating the vertical wind shear. However, in the present study, the upper-level circulation is maximal at 150 hPa. To better examine the effect of the background vertical wind shear on TC genesis, a spatial filtering technique is applied to separate the mesoscale vortex from the environmental circulation. Winds with wavelengths larger than 500 km are considered the background large-scale circulation, while winds with wavelengths smaller than 500 km represent the TC-scale vortex and smaller-scale convection. It is generally accepted that a strong vertical wind shear can inhibit TC development through the ventilation of moisture and energy away from the TC core region (e.g., Gray, 1968), or the entrainment of low-entropy air into the boundary layer (e.g., Riemer et al., 2009). The differences in the vertical zonal wind shear are closely associated with the development of vortices in these three experiments. The vertical zonal wind shear in SUA ranges from 6 m s^{-1} to 8 m s^{-1} after t = 66 h, whereas it varies between –2 m s^{-1} and 4 m s^{-1} in SLC, and the vertical zonal wind shear in CTL falls between 0 m s^{-1} and 6 m s^{-1}. Prior to t = 72 h, the vertical zonal wind shears in the three runs have prominent differences before the vortices start to intensify (Fig. 6 and Fig. 2). Note that the difference in the vertical zonal wind shear is not very sensitive to the size of the averaging box (such as 720 km × 720 km, 600 km × 600 km, and 450 km × 450 km) or to the use of spatial filtering (figures not shown).

The evolution of the vertical zonal wind shear depends closely on the zonal wind structures at the upper and lower levels, particularly the former. At the initial time, the upper-level anticyclonic circulation is approximately antisymmetric around the vortex center (Fig. 4d). At t = 72 h, the westerly winds to the north in SUA are the strongest among the three experiments at the upper level (Fig. 4e); these westerly winds are associated with the development of a beta gyre in the lower-level cyclonic circulation and the resultant asymmetry. A cyclonic circulation-induced beta gyre is a pair of vorticity anomalies with low vorticity to the northeast of the cyclone center and high vorticity to the southwest of the cyclone center at the lower level, leading to maximum winds located in the northeastern part of the vortex at the lower level (Holland, 1983; Fiornio and Elsberry, 1989; Wu and Emanuel, 1993, 1994). The strong winds in the northeastern quadrant of the vortex induce large surface heat fluxes (including sensible and latent heat fluxes) and thus higher humidity in the atmosphere (figure not shown). The near-surface inflow induced by friction further leads to ascending motion and more upward moisture transport, facilitating more convective heating in the region with the maximum wind and heat fluxes.

Figure 7 shows the 600-hPa geopotential height, sea level pressure (SLP), and 300-hPa vertical velocity fields in CTL, SUA, and SLC averaged over t = 60–72 h, 72–84 h, and 84–96 h. The major vertical motions are mostly located in the northeastern or southeastern quadrants of the vortex similar to the upper-level westerly winds. This suggests that the asymmetries of the vertical motion and associated diabatic heating play an important role in generating the upper-level asymmetric westerly flows. The diabatic heating in the northeastern quadrant of the vortex is associated with the upper-level outflows and divergent flows. In other words, the relatively large diabatic heating in the northeastern quadrant of the vortex generates anomalous southwesterly outflows around the vortex center at the upper level. With the effect of Earth's vorticity, the northwesterly winds beyond the vortex core are dominant at the upper level in the northeastern quadrant of the vortex as shown in Fig. 4. When the large-scale upper-level anticyclone is added into the CTL run, the large-scale anticyclone increases the westerly wind asymmetry to the north of the vortex, resulting in a larger vertical westerly wind shear than that in CTL, as shown in Fig. 6. The processes above are similar to those proposed by Li et al. (2014), who suggested that the asymmetries of the convection and associated diabatic heating induced by the land–sea surface contrast play a critical role in generating upper-level asymmetric westerly flows. Moreover, due to the weakest inertial instability at the upper level in SUA induced by strong anticyclonic flows, the outflow jet at the upper level extends over a greater horizontal distance than that at the lower level (Ge et al., 2010). It is worth noting that the vertical wind shear in the simulation is different from the beta shear, which results from the height-dependent advection of planetary vorticity (Wang and Holland, 1996a, 1996b; Ritchie and Frank, 2007; Fang and Zhang, 2012). These studies mainly examined the effect of the beta shear on the intensity of a mature TC. Ritchie and Frank (2007) indicated that the beta shear is mainly associated with the structure of the initial vortex, which consists of a cyclone in the lower level and an anticyclone in the upper level. In the present study, the vertical wind shear is mainly induced by the imposed large-scale anticyclonic circulation in the upper level.

Previous studies have shown that vertical wind shear can lead to the development of a forced secondary circulation with anomalous ascent on the downshear side and anomalous descent on the upshear side (e.g., Zhang and Kieu, 2006; Ge et al., 2013). These studies suggested that the ascending branch on the downshear side may reinforce itself through the release of latent heat by convection and enhance the secondary circulation; then, this enhanced secondary circulation could overcome the tilting induced by vertical wind shear and restore the vertical alignment, resulting in TC genesis (Ge et al., 2013). In contrast, some other studies suggested that a diabatically driven secondary circulation cannot directly maintain the vertical alignment of a mature TC (Jones, 2004; Reasor et al., 2004; Reasor and Eastin, 2012). These researchers indicated that an inviscid damping mechanism intrinsic to the dry adiabatic dynamics of a vortex is responsible for decreasing deviations from an upright state. To further examine how vertical wind shear makes a negative contribution to TC genesis, we investigate the vertical–zonal cross section of the meridional wind through the vortex center at t = 72 h, 84 h, and 96 h in CTL, SUA, and SLC (Fig. 8). At t = 72 h, the vortices more or less tilt eastward in the vertical direction under the beta-induced westerly shear that results from the height-dependent advection of the planetary vorticity (Figs. 8a, 8d, 8g). The tilt induced by the beta-induced shear might play a role in the early development of asymmetric convection. This eastward tilt is the most remarkable in SUA due to the strongest vertical zonal wind shear (Fig. 8d and Fig. 6). Twelve hours later, the vertical tilt decreases, and the vertical alignment of each vortex in CTL and SLC is gradually restored, with more evident vertical alignment in the latter (Figs. 8b, 8h). Accompanied by this vertical alignment, the vortices begin to intensify rapidly (Fig. 2). However, the vertical tilt persists in SUA during the following 12 h (Fig. 8e), indicating that the secondary circulation is not strong enough to restore the vertical alignment in SUA. At t = 96 h, the vortices become vertically aligned in CTL and SLC (Figs. 8c, 8i). The meridional wind, however, is much stronger in SLC than in CTL. In SUA, the meridional wind of the vortex is still characterized by an eastward tilt with height and a zonal asymmetric structure at the middle–lower levels at t = 96 h (Fig. 8f); as a result, the vortex develops slowly in SUA (Fig. 2).

As discussed above, strong vertical wind shear can ventilate moisture and energy away from the TC core region, inhibiting TC development (Gray, 1968). Figure 9 shows the time–azimuthal cross sections of the radial-mean (0–150 km) vertical motion at 300 hPa for CTL, SUA, and SLC from t = 60 h to t = 120 h. The 300-hPa level is chosen because the maximum vertical motion is located at this level. Before t = 90 h, the dominant vertical motions in the three runs are located in the northeastern and southeastern quadrants of the vortex. Among the three runs, the extents of the azimuthal coverage of the vertical motions are the smallest in SUA, indicating that the larger vertical wind shear in SUA makes a negative contribution to the frequency of the convective cells. After t = 90 h, convection starts to develop along the anti-clockwise direction of the vortex in CTL and SLC (Fig. 9a and Fig. 9c). In SLC, the vortex is almost completely wrapped by deep convection at t = 102 h, indicating that the asymmetries of the vertical motion and associated diabatic heating are remarkably decreased (Fig. 9c). In contrast, the vertical motion is still largely confined to the northeast and southeast quadrants of the vortex in SUA.

Figure 10 further shows the vertical-radial cross sections of the azimuthal-mean diabatic heating averaged over t = 60–72 h, 72–84 h, and 84–96 h in the three runs. At 60–72 h, the diabatic heating is generally similar among three runs (Figs. 10a, 10d, 10g). In the following 12 h, the differences in diabatic heating become evident among the three experiments. The convection in SLC is the most vigorous and is maximized at 500 hPa at a radius of approximately 30 km (Fig. 10h), while the convection in CTL is maximized at a radius of 50 km at the same level but with a relatively weak magnitude (Fig. 10b). In contrast, the diabatic heating in SUA is the weakest and is located at the vortex center (Fig. 10e), which may be due to the absence of a clear eye region and the tilt of the heating structure in the weak vortex. At 84–96 h, greater diabatic heating is promoted in all three cases when the vertical alignment of the vortices is restored gradually, as shown in Fig. 8. The heating structure in SLC (Fig. 10i) bears a characteristic convective precipitation regime (Mapes and Houze, 1995), while the convective heating in CTL intensifies and contracts from a radius of 50 km to 20 km (Figs. 10b–c). In contrast, the heating in SUA has a relatively larger size, indicating that the TC is characterized by a less contracted vortex (Fig. 10f). The results shown in Figs. 9 and 10 indicate that a strong vertical zonal wind shear can induce slow vortex development by ventilating energy away from the inner core during the early stage of TC genesis.

To support the physical mechanisms that we propose, two groups of additional sensitivity experiments are performed. The first group of experiments is similar to the SUA case except that the initial specific humidity is decreased by 50% to examine the impact of the moisture. This experiment is called SUAdry50. As expected, the development of the vortex is slower in SUAdry50 than in SUA and CTL due to the decrease in moisture (Fig. 11). Furthermore, we compare the surface latent and sensible heat fluxes and the vertical structure of the vortex between SUA and SUAdry50. The asymmetric surface heat fluxes in SUAdry50 appear at t = 72 h and then intensify at t = 84 h and t = 96 h (Figs. 12a-c). It is worth noting that the vortex does not show an obvious tilt at t = 72 h in SUAdry50 (Fig. 12d). The vortex has a similar vertical tilt at t = 60 h as at t = 72 h (figure not shown). With an increase in the asymmetric surface heat fluxes, the eastward tilt in SUAdry50 increases remarkably after t = 84 h (Figs. 12e-f). Due to the decreased of moisture content in the atmosphere, the development of convection and the occurrence of vertical tilting are delayed in SUAdry50 compared to SUA (Fig. 8 and Fig. 12). The comparison between SUA and SUAdry50 indicates that the vertical wind shear and vertical tilt do not develop earlier than the asymmetry of surface heat fluxes. The SUAdry50 sensitivity experiment supports the hypothesis that the vertical tilt of the vortex is induced by the asymmetries of the surface fluxes and associated diabatic heating.

The second group of experiments is similar to CTL and SUA except that these experiments are conducted on an f plane at 15 °N and are thus called CTL_f and SUA_f, respectively. Due to the existence of the f plane, the beta gyres are eliminated, and thus, the anticyclone in the upper level is well maintained (figure not shown). Figure 13 shows that the development of the vortex in SUA_f is almost similar to that of the vortex in CTL_f, indicating that the well-organized upper-level anticyclone does not detrimentally affect tropical cyclogenesis. Through a comparison with the simulation results on the beta plane, we conclude that the establishment and development of the beta gyre and the evolution and deformation of the upper-level anticyclonic circulation on the beta plane together result in a large vertical wind shear, which is unfavorable to tropical cyclogenesis. The mechanisms by which the vortices in SUA_f and CTL_f have similar genesis times will be investigated in future work.

3.3. Lower-level cyclonic circulation

As Fig. 2 shows, the modeling results indicate that the vortex has a large intensification rate under the lower-level cyclonic circulation. Thus, to examine how the lower-level cyclonic circulation makes a positive contribution to TC genesis, we first investigate the time evolutions of the area-averaged tangential wind, surface heat flux, relative humidity, and diabatic heating from t = 48 h to t = 96 h in CTL, SUA and SLC (Fig. 14). It is clearly seen that the superposition of the vortex and the large-scale cyclonic circulation at the lower level enhances the tangential wind in the core (Fig. 14b), which induces greater surface heat fluxes (including both sensible and latent heat fluxes) in SLC than in CTL and SUA (Fig. 14c), leading to the upward extension of high humidity. As a result, the vertically averaged magnitude of relative humidity is greater in SLC than in CTL and SUA (Fig. 14c), which is favorable for the development of convection reflected by the vertically integrated diabatic heating (Fig. 14d). As shown in Fig. 9, the extent of the azimuthal coverage of strong vertical motion is the greatest in SLC, reflecting the occurrence of more convective bursts inside or near the maximum wind radius.

Previous studies showed that convective cells could experience progressive organization and aggregation toward the vortex center (Ge et al. 2013). Schecter and Dubin (1999) showed that vorticity anomalies generated by small convective cells could segregate under the influence of the ambient radial vorticity gradient. That is, positive vorticity can move up and negative vorticity can move down along the gradient of ambient vorticity, resulting in the separation of positive and negative vorticities. Figure 15 shows the horizontal distribution of the relative vorticity for the small-scale system and large-scale system in CTL and SLC from t = 78 h to t = 108 h at an interval of 6 h by using the Fourier spatial filtering technique. Compared with CTL, the positive convectively generated vorticity anomalies have a faster build-up in SLC at t = 84 h (Fig. 15b and Fig. 15h), and subsequently, more small-scale vorticity anomalies aggregate toward the center region of the vortex in SLC (Figs. 15d-f and Figs. 15j-l). Ge et al. (2015) suggested that a larger ambient vorticity gradient is more favorable for a quicker segregation process. Therefore, we further display in Fig. 16 the radial profiles of the azimuthal-mean relative vorticity and the related vorticity gradient near the TC center during the early stage of TC genesis. Consistent with the earliest genesis of TC, the relative vorticity and the radial vorticity gradient are the largest in SLC among the three cases, which leads to a quicker TC genesis.

As an indicator of the potential for TC development, the Okubo–Weiss (OW) parameter is examined to measure the effect of horizontal flow deformation. At the middle level, large deformed flows can facilitate the penetration of surrounding dry air into the core of a vortex, suppressing TC development (Dunkerton et al., 2009; Raymond et al., 2011; Ge et al., 2013). This process is thought to inhibit increase in moisture and convection, necessary for the spin-up of the lower-level vortex (Nolan, 2007). Following Raymond et al. (2011), the normalized OW parameter is defined as

$$\mathrm{OW} = \frac{\varsigma^2-\sigma_1^2-\sigma_2^2}{\varsigma^2+\sigma_1^2+\sigma_2^2},$$

where

$$\varsigma = \frac{\partial v}{\partial x} - \frac{\partial u}{\partial y}, \sigma_1 = \frac{\partial v}{\partial x} + \frac{\partial u}{\partial y}, \sigma_2 = \frac{\partial u}{\partial x} - \frac{\partial v}{\partial y}.$$

The above parameter is expressed in the form of the square of the relative vorticity minus the squares of the two strain rate components. The parameter equals 1 when the flow is completely rotational and –1 when the flow is totally strained. Generally, the maxima of the OW parameter are located around the inner core of the vortex. Figure 17 depicts the evolution of the area-averaged (60 km × 60 km) OW parameter in vertical-time cross sections from t = 72 h to t = 120 h following the vortex center in the three experiments. The value of the OW parameter in

SLC is much greater and more positive in the middle troposphere than in the other two experiments. This indicates that rotational flows dominate over strained flows in SLC, which inhibit the entrainment of dry air into the core of the vortex region (Raymond et al., 2011).

Note that Xu et al. (2016) found that a vortex does not experience a quicker genesis when a TC is embedded into a monsoon gyre. They demonstrated that the superposition of a vortex and a large-scale monsoon gyre produces a vortex with a larger outer size, which is not conducive to the rapid development of the vortex (Xu and Wang, 2018). However, in our study, the superposition of a vortex and a large-scale cyclonic circulation at the lower level does not lead to an obvious increase in the maximum wind radius except for a salient increase in the tangential wind near and outside the maximum wind radius (Fig. 18). Our simulation results show that increasing the tangential wind near and outside the maximum wind radius can result in greater surface heat fluxes in SLC, which is favorable for the development of convection in the core of the vortex (Fig. 14). Thus, it is inferred that the positive contribution of the large-scale cyclonic circulation to the development of the vortex may be greater than the negative contribution due to the large initial size. However, the simulation result may be sensitive to the size of the large-scale cyclonic circulation, which will be further investigated in future work.

3.4. Sensitivity experiments

To examine the sensitivity of vortex development to the upper-level anticyclonic circulation structure, a third group of additional experiments is designed (see Table 1). In this group, four experiments are carried out. The experiments are the same as SUA except for differences in the vertical height, radius, and intensity of the maximum tangential wind of the upper-level anticyclonic circulation. Only one parameter of the maximum tangential wind is modified in each additional experiment relative to the parameters in SUA. In the first and second experiments (SUA_P250 and SUA_P100, respectively), the maximum upper-level anticyclonic circulation is set at 250 hPa and 100 hPa, respectively. In the third experiment (SUA_R400), the initial maximum tangential wind of the upper-level anticyclonic circulation is located at a radius of 400 km. In the fourth experiment (SUA_V16), the initial maximum tangential wind of the upper-level anticyclonic circulation is set to 16 m s^{-1}.

Figure 19 shows the time evolutions of the MSLP in CTL, SUA, SUA_P250, SUA_P100, SUA_R400, and SUA_V16. It is seen that the development of the vortex influenced by the upper-level anticyclonic circulation is not highly sensitive to the vertical height, radius, and magnitude of the maximum tangential wind of the upper-level anticyclonic circulation. Compared with that in CTL, the upper-level anticyclonic circulations in the additional experiments have a consistently negative effect on the rapid development of the vortex. The evolutions of the wind field at 150 hPa in SUA_P250, SUA_R400, and SUA_V16 (shown in Fig. 20) are also examined and compared with the evolution of that in SUA. At the initial time, the winds at 150 hPa are very weak in SUA_P250 (Fig. 20a), whereas strong anticyclonic circulations are seen in SUA_R400 and SUA_V16, with stronger winds covering broader extents in the latter (Figs. 20d and 20g). At t = 72 h, the westerly wind development to the north-northeast in these three experiments is associated with the lower-level beta gyre and the asymmetries of the vertical motion and diabatic heating, as discussed in section 3.2. At t = 120 h, the westerly winds poleward of the vortex center intensify and dominate on the northeastern side of the vortex center in these three runs (Figs. 20c, 20f, and 20i). The westerly wind evolutions in all three experiments are similar to those in SUA (Fig. 20 and Figs. 4d–f). As a result, a relatively strong vertical wind shear is induced, which slows down the development of the vortex as discussed in section 3.2. The simulation results indicate that the upper-level anticyclonic circulation makes a negative contribution to the development of the vortex compared with CTL regardless of the vertical height, radius and magnitude of the maximum tangential wind of the upper-level anticyclonic circulation. This conclusion agrees with the finding of Xu et al. (2016), who showed that an upper-level circulation associated with a monsoon gyre is not conducive to the development of a vortex.

Additional sensitivity experiments are performed to examine the statistical significance of the simulation results related to the initial conditions in the CTL and SLC cases. Five three-dimensional random disturbances with the magnitude less than 10^{-2} m s^{-1} are added into the zonal wind fields in the CTL and SLC cases at the initial time, respectively. The black and red solid lines in Fig. 21 show the time evolutions of the averaged MSLP in the vortex in all the CTL and SLC experiments, respectively. As shown in Fig. 21, the simulation results are not so sensitive to the initial conditions, confirming that the development of the vortex initialized with the large-scale lower-level cyclone invariably occurs faster than the development of the vortex in the control simulation.

4. Summary and discussion

Previous studies on the effect of an upper-level circulation on the development of a vortex were mainly focused on the intensity and structural changes of a mature TC, not on TC genesis. Some earlier studies suggested that both an upper-level anticyclonic circulation and a lower-level cyclonic circulation are necessary conditions for TC formation. However, most of these studies were confined to composite analyses based on observational data. The present study conducts further research to quantify the contributions of an upper-level anticyclonic circulation and a lower-level cyclonic circulation to TC genesis through idealized numerical experiments using a mesoscale WRF model.

Model results show that given a specified weak vortex, an upper-level anticyclonic circulation can result in the slower formation of a TC compared to CTL. This can be mainly ascribed to the zonal wind structures at the upper level, which are associated with the development of beta gyres in the lower-level cyclonic circulation and the resultant asymmetries of convection. A cyclonic-circulation-induced beta gyre leads to maximum winds located in the northeastern part of the vortex center at the lower level; these winds induce strong surface heat fluxes and thus higher humidity in the atmosphere. The near-surface inflow induced by friction leads to ascending motion and increases upward transport of moisture, facilitating more convective heating in the region of the maximum wind and heat fluxes. The diabatic heating in the northeastern quadrant of the vortex generates anomalous northwesterly winds beyond the vortex core at the upper level. The large-scale anticyclone at the upper level increases the asymmetry of the westerly wind to the north of the vortex, resulting in a relatively large vertical westerly wind shear, which is regarded as an unfavorable factor for TC formation. As a result, the upper-level vortex shifts eastward from its original position, which is unfavorable for the vertical alignment of the vortex. The forced secondary circulation has to take more time to help overcome the shear-induced drifting effect and restore the vertical alignment of the vortex. Therefore, an upper-level anticyclonic circulation is indeed detrimental to TC formation.

In contrast, a lower-level cyclonic circulation can result in the faster formation of a TC due to the superposition of large-scale cyclonic vorticity and a vortex. The overlying strong wind induces large surface heat fluxes from the ocean and the convergence of moisture from the surrounding environment. In a moist environment, convection and diabatic heating can be strengthened. A greater initial absolute vorticity effectively enhances convection–circulation–moisture positive feedback. Moreover, a greater OW parameter reveals the dominance of rotation over strain, which could inhibit the penetration of dry environmental air into the core region of the vortex at the middle level. These factors are indicators of the potential for vortex intensification.

In this study, we mainly focus on the separate roles of an upper-level anticyclonic circulation and a lower-level cyclonic circulation. In the future, we will carry out a series of sensitivity experiments to investigate the sensitivity of vortex development to large-scale circulations with different sizes and magnitudes. Meantime, the location of the upper-level anticyclonic circulation may vary horizontally depending on environmental factors. The study of MZ81 mentioned that a cloud cluster developing into a tropical cyclone have an anticyclone displaced ~3 degree latitude to the east of the system. Therefore, it is necessary to investigate the sensitivity of vortex development to the relative location of the upper-level anticyclonic circulation with respect to the vortex core in future research.

Acknowledgments. The first author, Dr. Xi Cao, thanks Prof. Guanghua Chen and Prof. Chun-Chieh Wu for their constructive suggestions, which helped improve the paper. We also appreciate the comments from the editor and three anonymous reviewers. The simulation data are generated using the WRF model (version 3.3.1), which are available upon request to the first author by email at caoxi09@mail.iap.ac.cn. This study was supported by the 2019 Open Research Program of the Shanghai Typhoon Institute (Grant TFJJ201901), the Open Grants of the State Key Laboratory of Severe Weather (Grant 2020LASW-B01) and the National Natural Science Foundation of China (Grant 41505048 and 41875057).

References

Bister, M., and K. A. Emanuel, 1997: The genesis of Hurricane Guillermo: TEXMEX analyses and a modeling study, *Mon. Wea. Rev.*, **125**, 2662–2682.

Cao, X., P. Huang, G. H. Chen, and W. Chen, 2012: Modulation of western North Pacific tropical cyclone genesis by intraseasonal oscillation of ITCZ: A statistical analysis, *Adv. Atmos. Sci*., **29**, 744–754.

Cao, X., T. Li, M. Peng, W. Chen, and G. H. Chen, 2014a: Effects of monsoon trough intraseasonal oscillation on tropical cyclogenesis over the western North Pacific, *J. Atmos. Sci*., **71**, 4639–4660.

Cao, X., T. Li, M. Peng, W. Chen, and G. H. Chen, 2014b: Effects of monsoon trough interannual variation on tropical cyclogenesis over the western North Pacific, *Geophys. Res. Lett*., **41**, 4332–4339.

Cao, X., G. H. Chen, T. Li, F. M. Ren, 2016: Simulations of tropical cyclogenesis associated with different monsoon trough patterns over the western North Pacific, *Meteor. Atmos. Phys.*, **128**, 491–511, doi: 10.1007/s00703-015-0428-7.

Cao, X., and R. G. Wu, 2018a: Simulations of development of tropical disturbances associated with the monsoon trough over the western North Pacific. *Atmos. Sci. Lett.*, **19**(2), doi: 10.1002/asl.801.

Cao, X., and R. G. Wu, 2018b: Comparison of different time scale contributions to tropical cyclone genesis over the Western North Pacific in 2015 and 2016, *J. Meteor. Soc. Japan,* **96**(4), 317–336.

Cao, X., R. G. Wu, and M. Y. Bi, 2018: Contributions of different time scale variations to tropical cyclogenesis over the western North Pacific. *J. Climate*, **31**, 3137–3153, doi:

10.1175/JCLI-D-17-0519.1.

Cao, X., R. G. Wu, N. Wei, and Y. F. Dai, 2020: Location of the preferred region for tropical cyclogenesis in strong monsoon trough pattern over the western North Pacific, *J. Meteor. Soc. Japan*, **98**, doi: 10.2151/jmsj. 2020-034.

DeMaria, M., J. J. Baik, and J. Kaplan, 1993: Upper-level angular momentum fluxes and tropical cyclone intensity change, *J. Atmos. Sci*., **50**, 1133–1147.

Dunkerton, T. J., M. T. Montgomery, and Z. Wang, 2009: Tropical cyclogenesis in a tropical wave critical layer: Easterly waves, *Atmos. Chem. Phys.*, **9**, 5587–5646.

Fang, J., and F. Zhang, 2010: Initial development and genesis of Hurricane Dolly (2008), *J. Atmos. Sci*, **67**, 655–672.

Fang, J., and F. Zhang, 2012: Effect of beta shear on simulated tropical cyclones. *Mon. Wea. Rev.*, **140**, 3327–3346

Feng, T., G. H. Chen, R. H. Huang, and X. Y. Shen, 2014: Large-scale circulation patterns favorable to tropical cyclogenesis over the western North Pacific and associated barotropic energy conversions, *Int. J. Climatol*., **34**, 216–227.

Fiorino, M., and R. L. Elsberry, 1989: Some Aspects of vortex structure related to tropical cyclone motion, *J. Atmos. Sci.*, **46**, 975–990

Fritz, C., and Z. Wang, 2013: A numerical study of the impacts of dry air on tropical cyclone formation: a development case and a nondevelopment case, *J. Atmos. Sci*., **70**, 91–111.Fu, B., M. S. Peng, T. Li, and D. E. Stevens, 2012: Developing versus nondeveloping disturbances for tropical cyclone formation. Part II: western North Pacific, *Mon. Wea. Rev.*, **140**, 1067–1080.

Ge, X. Y., T. Li, and M. Peng, 2010: Cyclogenesis simulation of typhoon Prapiroon (2000) associated with Rossby wave energy dispersion, *Mon. Wea. Rev*., **138**, 42–54.

Ge, X. Y., T. Li, and M. Peng, 2013: Effects of vertical shears and midlevel dry air on tropical cyclone developments, *J. Atmos. Sci*., **70**, 3859–3875.

Ge, X., Xu, W. and Zhou, S.W., 2015: Sensitivity of tropical cyclone intensification on initial inner-core structure. *Adv. Atmos. Sci.*, **32**(10), 1407–1418.

Gray, W. M., 1968: Global view of the origin of tropical disturbances and storms, *Mon. Wea. Rev.*, **96**, 669–700.

Gray, W. M., 1998: The formation of tropical cyclones, *Meteorol. Atmos. Phys*., **67**, 37–69.

Holland, G. J., 1983: Tropical cyclone motion: environmental interaction plus a beta effect, *J. Atmos. Sci.*, **40**, 328–342.

Holland, G. J., 1997: The maximum potential intensity of tropical cyclones, *J. Atmos. Sci.*, **54,** 2519–2541.

Holland, G. J., and R. T. Merrill, 1984: On the dynamics of tropical cyclone structure changes, *Q. J. R. Meteor. Soc.*, **110**, 723–745.

Jones, S. C., 2004: On the ability of dry tropical-cyclone-like vortices to withstand vertical shear, *J. Atmos. Sci.*, **61**, 114–119.

Kain, J. S., and J. M. Fritsch, 1993: Convective parameterization for mesoscale models: The Kain–Fritsch scheme. The representation of cumulus convection in numerical models, Meteor. Monogr., No.46, Amer. Meteor. Soc., 165–170.

Lee, C. S., K. W. Kevin, J. S. Cheung, N. Hui, R. and L. Elsberry, 2008: Mesoscale features associated with tropical cyclone formations in the western North Pacific, *Mon. Wea. Rev*., **136**, 2006–2022.

Leroux, M. D, M. Plu, D. Barbary, F. Roux, and P. Arbogast, 2013: Dynamical and physical processes leading to tropical cyclone intensification under upper-level trough forcing, *J. Atmos. Sci*., **70**, 2547–2565.

Li, T., 2012: Synoptic and climatic aspects of tropical cyclogenesis in western North Pacific. Nova Science Publishers, Inc., Eds. K. Oouchi and H. Fudeyasu, Chap.3, 61–94.

Li, Y. B., K. K. W. Cheung and J. C. L. Chan, 2014: Numerical study on the development of asymmetric convection and vertical wind shear during tropical cyclone landfall, *Q. J. R. Meteorol. Soc.*, **140**, 1866–1877.

Lin, Y. L., R. D. Farley, and H. D. Orville, 1983: Bulk parameterization of the snow field in a cloud model, *J. Appl. Meteor*., **22**, 1065–1092.

Mapes, B. E., and R. A. Houze, 1995: Diabatic divergence profiles in Western Pacific mesoscale convective systems, *J. Atmos. Sci*., **52**, 1807–1828.

McBride, J. L., and R. Zehr, 1981: Observational analysis of tropical cyclone formation. Part II: Comparison of non-developing versus developing systems, *J. Atmos. Sci*., **38**, 1132–1151.

Merrill, R. T., 1988: Environmental influences on hurricane intensification, *J. Atmos. Sci*., **45**, 1678–1687.

Montgomery, M. T., M. E. Nicholls, T. A. Cram, and A. Saunders, 2006: A vortical hot tower route to tropical cyclogenesis, *J. Atmos. Sci*., **63**, 355–386.

Nolan, D. S., 2007: What is the trigger for tropical cyclogenesis? *Aust. Meteor. Mag*., **56**, 241–266.

Rappin, E. D., M. C. Morgan, and G. J. Tripoli, 2011: The impact of outflow environment on tropical cyclone intensification and structure, *J. Atmos. Sci.*, **68**, 177–194.

Raymond, D. J., S. L. Sessions, and C. Lopez Carrillo, 2011: Thermodynamics of tropical cyclogenesis in the northwest Pacific, *J. Geophys. Res*., **116**, D18101, doi:

10.1029/2011JD015624.

Reasor, P. D., M. T. Montgomery, and L. D. Grasso, 2004: A new look at the problem of tropical cyclones in vertical shear flow: Vortex resiliency, *J. Atmos. Sci.*, **61**, 3–22.

Reasor, P. D., and M. D. Eastin, 2012: Rapidly intensifying hurricane Guillermo, 1997: Part II: Resilience in shear, *Mon. Wea. Rev*., **140**, 425–444.

Riemer, M., M. T. Montgomery, and M. E. Nicholls, 2009: A new paradigm for intensity modification of tropical cyclones: Thermodynamic impact of vertical wind shear on the inflow layer, *Atmos. Chem. Phys.*, **10**, 3163–3188.

Ritchie, E. A., and G. J. Holland, 1997: Scale interactions during the formation of Typhoon Irving, *Mon. Wea. Rev*., **125**, 1377–1396.

Ritchie, E. A., and G. J. Holland, 1999: Large-scale patterns associated with tropical cyclogenesis in the western Pacific, *Mon. Wea. Rev*., **127**, 2027–2043.

Ritchie, E. A. and W. M. Frank, 2007: Interactions between simulated tropical cyclones and an environment with a variable Coriolis parameter. *Mon. Wea. Rev*., **135**, 1889–1905.

Sadler, J. C., 1976: A role of the tropical upper tropospheric trough in early season typhoon development, *Mon. Wea. Rev*., **104**, 1266–1278.

Schecter, D. A. and D. H. Dubin, 1999: Vortex motion driven by a background vorticity gradient. *Phys. Rev. Lett*, **83**, 2191–2194.

Schubert, W. H., and J. J. Hack, 1982: Inertial stability and tropical cyclone development, *J. Atmos. Sci*., **39**, 1687–1697.

Skamarock, W. C., J. B. Klemp, J. Dudhia, D. O. Gill, D. M. Barker, M. G. Duda, X. Y. Huang, W. Wang, and J. G. Powers, 2008: A description of the advanced research WRF version 3. NCAR Technical note NCAR/TN-475+STR.

Wang, Y. Q., 1995: On an inverse balance equation in sigma-coordinates for model initialization, *Mon. Wea. Rev*., **123**, 482–488.

Wang, Y. Q., 1998: On the bogusing of tropical cyclones in numerical models: The influence of vertical structure, *Meteor. Atmos. Phys*., **65**, 153–170.

Wang, Y. Q. and Holland, G. J., 1996a: The beta drift of baroclinic vortices. Part I: Adiabatic vortices. *J. Atmos. Sci*., **53**, 411–427.

Wang, Y. Q. and Holland, G. J., 1996b: The beta drift of baroclinic vortices. Part II: Diabatic vortices. *J. Atmos. Sci*., **53**, 3737–3756.

Wang, Z., 2014: Role of cumulus congestus in tropical cyclone formation in a high-resolution numerical model simulation, *J. Atmos. Sci*., **71**, 1681–1700.

Wu, C. C., and K. A. Emanuel, 1993: Interaction of a baroclinic vortex with background shear: Application to hurricane movement, *J. Atmos. Sci*., **50**, 62–76.

Wu, C. C., and K. A. Emanuel, 1994: On hurricane outflow structure, *J. Atmos. Sci*., **51**, 1995–2003.

Wu, L. G., H. J. Zong, and J. Liang, 2013: Observational analysis of tropical cyclone formation associated with monsoon gyres, *J. Atmos. Sci*., **70**, 1023–1034.

Xu, M. T., S. W. Zhou, and X. Y. Ge, 2016: An idealized simulation study of monsoon gyre on tropical cyclogenesis, *Acta. Meteor. Sin.*, **74**, 733–743.

Xu, J., and Y. Q. Wang, 2018: Effect of the Initial Vortex Structure on Intensification of a Numerically Simulated Tropical Cyclone, *J. Meteor. Soc. Japan*, **96**, 111–126.

Yan, Z, X. Y. Ge, M. Peng, and T. Li, 2019: Does monsoon gyre always favour tropical cyclone rapid intensification? *Q. J. R. Meteor. Soc*., 1–13. https://doi.org/10.1002/qj.3586

Zehr, R. M., 1992: Tropical cyclogenesis in the western North Pacific. NOAA Tech. Rep.

NESDIS 61, Department of Commerce, Washington DC, 181pp.

Zhang, D. L., and C. Q. Kieu, 2006: Potential vorticity diagnosis of a simulated hurricane. Part II: Quasi-balanced contributions to forced secondary circulations, *J. Atmos. Sci*., **63**, 2898–2914.

Table and Figure Captions

Table 1. Model experiment descriptions. “S” denotes a sensitivity experiment.

Figure 1. The (a-c) 150-hPa and (d-f) 850-hPa wind fields (vectors) of the initial vortices in (a, d) CTL, (b, e) SUA and (c, f) SLC. Vertical-radial cross sections of the azimuthal-mean tangential wind (m s^{-1}) for the initial vortices in (g) CTL, (h) SUA, and (i) SLC.

Figure 2. The time evolutions of (a) the MSLP (hPa) and (b) the MAMW speed (m s^{-1}) at the 10 m height in four experiments CTL (black), SUA (red), SLC (blue), and SUALC (green).. The abscissa represents time (hour), and while the ordinate corresponds to the value of intensity. The dashed line in (b) denotes the TC genesis time when the MAMW speed exceeds 15 m s^{-1}.

Figure 3. The vertical–radial cross sections of the azimuthal mean tangential wind (contours, m s^{-1}) and diabatic heating (shaded, 10^{-3} K s^{-1}) in (a) CTL, (b) SUA), and (c) SLC at t = 120 h. (d–f) The same as in Figs. 3a–c except for the radial wind (contours, m s^{-1}).

Figure 4. The wind vectors and zonal velocities (shaded) at 150 hPa in (a–c) CTL, (d–f) SUA, and (g–i) SLC at t = 0 h (left), 72 h (middle), and 120 h (right) from the 27km simulation.

Figure 5. The same as in Fig. 4 but at 850 hPa.

Figure 6. The area-averaged (720 km × 720 km) vertical zonal wind shear (150–850 hPa) of CTL (black), SUA (red), and SLC (blue) from t = 0 h to t = 96 h.

Figure 7. The 600-hPa geopotential height (blue dashed contours), SLP (black solid contours), and 300-hPa vertical velocity fields (shading) in (a–c) CTL, (d–f) SUA, and (g–i) SLC averaged over t = 60–72 h (left), 72–84 h (middle), and 84–96 h (right).

Figure 8. The vertical–zonal cross sections of the meridional wind (m s^{-1}) in (a–c) CTL, (d–f) SUA, and (g–i) SLC at t = 72 h (left), 84 h (middle), and 96 h (right).

Figure 9. The time–azimuthal cross sections of the radial-mean (0–150 km) vertical motion (m s^{-1}) at 300 hPa for CTL, SUA, and SLC from t = 60 h to t = 120 h.

Figure 10. The vertical–radial cross sections of the azimuthal-mean diabatic heating (10^{-4} K s^{-1}) in (a–c) CTL, (d–f) SUA, and (g–i) SLC averaged over 60–72 h (left), 72–84 h (middle), and 84–96 h (right).

Figure 11. The time evolutions of the MSLP (hPa) in three experiments: CTL (black), SUA (red), and SUAdry50 (blue). The abscissa represents time (h), and the ordinate corresponds to the intensity of the MSLP.

Figure 12. The surface heat fluxes (unit: W m^{-1}) and 10-m winds at (a) t = 72 h, (b) t = 84 h and (c) t = 96 h in SUAdry50. (d-f) The same as in (a-c) except for the vertical–zonal cross sections of the meridional wind (m s^{-1}).

Figure 13. The time evolutions of the MSLP (hPa) in two experiments, CTL_f (black) and SUA_f (red), on an f plane at 15°N. The abscissa represents time (h), and the ordinate corresponds to the intensity.

Figure 14. The time evolutions (24-h running mean) of the (a) radial-mean (0-180 km) tangential wind (m s^{-1}) at 10 m, (b) radial-mean (0-360 km) surface heat flux (W m^{-2}), (c) radial-mean (0-180 km) and vertically averaged (1000-300 hPa) relative humidity (%),, and (d) vertically averaged (1000-200 hPa) diabatic heating (10^{-4} K s^{-1}) in CTL (black), SUA (red), and SLC (blue) from t = 48 h to t = 96 h.

Figure 15. The horizontal distributions of the relative vorticity for the small-scale system (contours, beginning from 3×10^{-5} s^{-1} at an interval of 1×10^{-5} s^{-1}) and the large-scale system (shading, at an interval of 1×10^{-5} s^{-1}) in the (a-f) CTL and (g-l) SLC cases from t = 78 h to t = 108 h at an interval of 6 h. The red box denotes the center region of the vortex.

Figure 16. The radial distributions of (a) the relative vorticity (10^{-5} s^{-1}) and (b) the associated 27-km running mean gradient of the relative vorticity (-d(Vor)/dR, 10^{-9} s^{-1} m^{-1}) at 850 hPa in CTL (black line), SUA (red line), and SLC (blue line) averaged from t = 72 h to t = 84 h.

Figure 17. The vertical–time cross sections of the area-averaged OW parameter (60 km × 60 km) from t = 72 h to t = 120 h in (a) CTL, (b) SUA and (c) SLC.

Figure 18. The radial distributions of the azimuthal-mean tangential wind of the vortex at the surface (m s^{-1}) in CTL (black), SUA (red), and SLC (blue) at the initial time.

Figure 19. The time evolutions of the (a) MSLP (hPa) and (b) MAMW (m s^{-1}) in CTL (black), SUA (red), SUA_P250 (blue), SUA_P100 (green), SUA_R400 (orange), and SUA_V16 (purple). The abscissa represents the integration time (h), and the ordinate corresponds to the intensity. The dashed line in (b) denotes the TC genesis time when the MAMW speed exceeds 15 m s^{-1}.

Figure 20. The same as in Fig. 4 but in (a–c) SUA_P250, (d–f) SUA_R400, and (g–i) SUA_V16.

Figure 21. The time evolutions of the MSLP (hPa) in the ensemble experiments of the CTL case (black) and SLC case (red). The abscissa represents time (h) and the ordinate corresponds to the intensity.

Table 1. Model experiment descriptions. “S” denotes a sensitivity experiment.

Experiment name	Description
CTL	Initial vortex with a maximum tangential wind of 8 m s^{-1} at a radius of 150 km at the surface with the vertical profile of a sine function in a resting environment
SUA	Similar to CTL except with a strong upper-level anticyclonic circulation with a maximum tangential wind of 8 m s^{-1} at a radius of 700 km at 150 hPa
SLC	Similar to CTL except with a strong lower-level cyclonic circulation with a maximum tangential wind of 8 m s^{-1} at a radius of 700 km at the surface
SUALC	Similar to CTL except with both a lower-level cyclonic circulation and an upper-level anticyclonic circulation
CTL_f	Similar to CTL except on an f plane
SUA_f	Similar to SUA except on an f plane
SUAdry50	Similar to SUA except that the initial specific humidity is decreased by 50%
SUA_P250	Similar to SUA except for the maximum tangential wind of the upper-level anticyclonic circulation being at 250 hPa
SUA_P100	Similar to SUA except for the maximum tangential wind of the upper-level anticyclonic circulation being at 100 hPa
SUA_R400	Similar to SUA except for the maximum tangential wind of the upper-level anticyclonic circulation being at a radius of 400 km
SUA_V16	Similar to SUA except for the upper-level anticyclonic circulation having a maximum tangential wind of 16 m s^{-1}

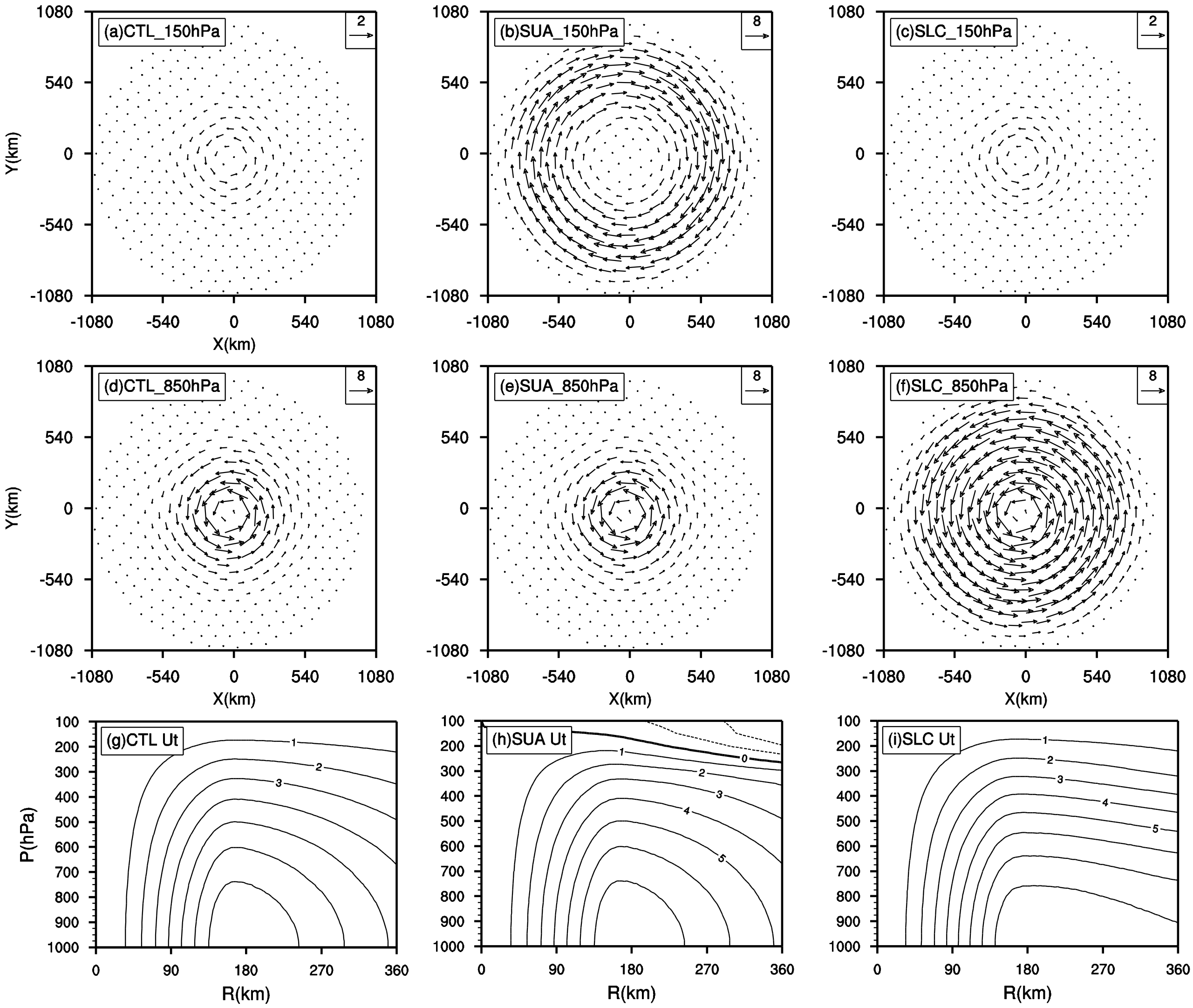

Figure 1. The (a-c) 150-hPa and (d-f) 850-hPa wind fields (vectors) of the initial vortices in (a, d) CTL, (b, e) SUA and (c, f) SLC. Vertical-radial cross sections of the azimuthal-mean tangential wind (m s^{-1}) for the initial vortices in (g) CTL, (h) SUA, and (i) SLC.

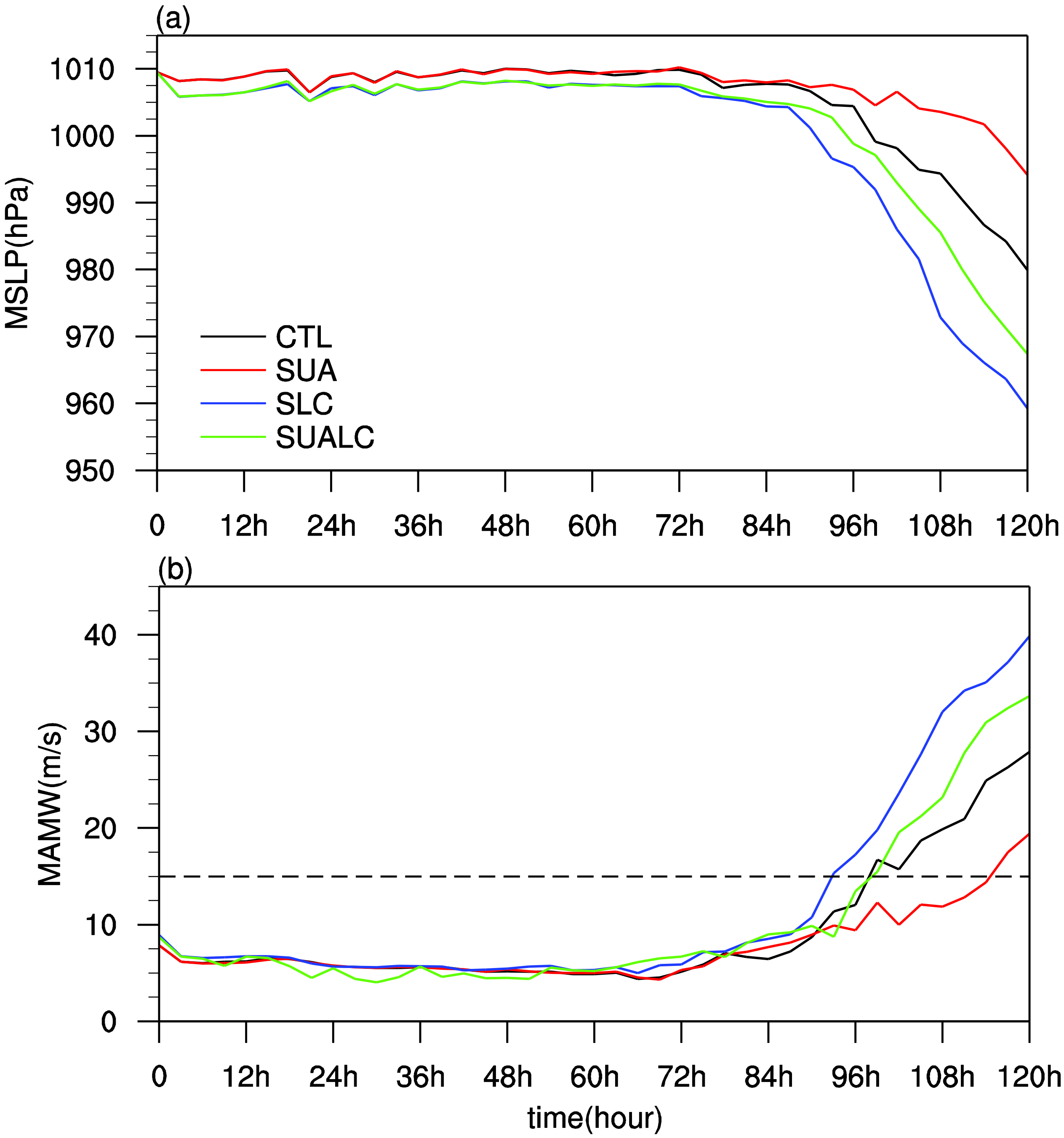

Figure 2. The time evolutions of (a) the MSLP (hPa) and (b) the MAMW speed (m s^{-1}) at 10 m in four experiments: CTL (black), SUA (red), SLC (blue), and SUALC (green). The abscissa represents time (h), and the ordinate corresponds to the intensity. The dashed line in (b) denotes the TC genesis time when the MAMW speed exceeds 15 m s^{-1}.

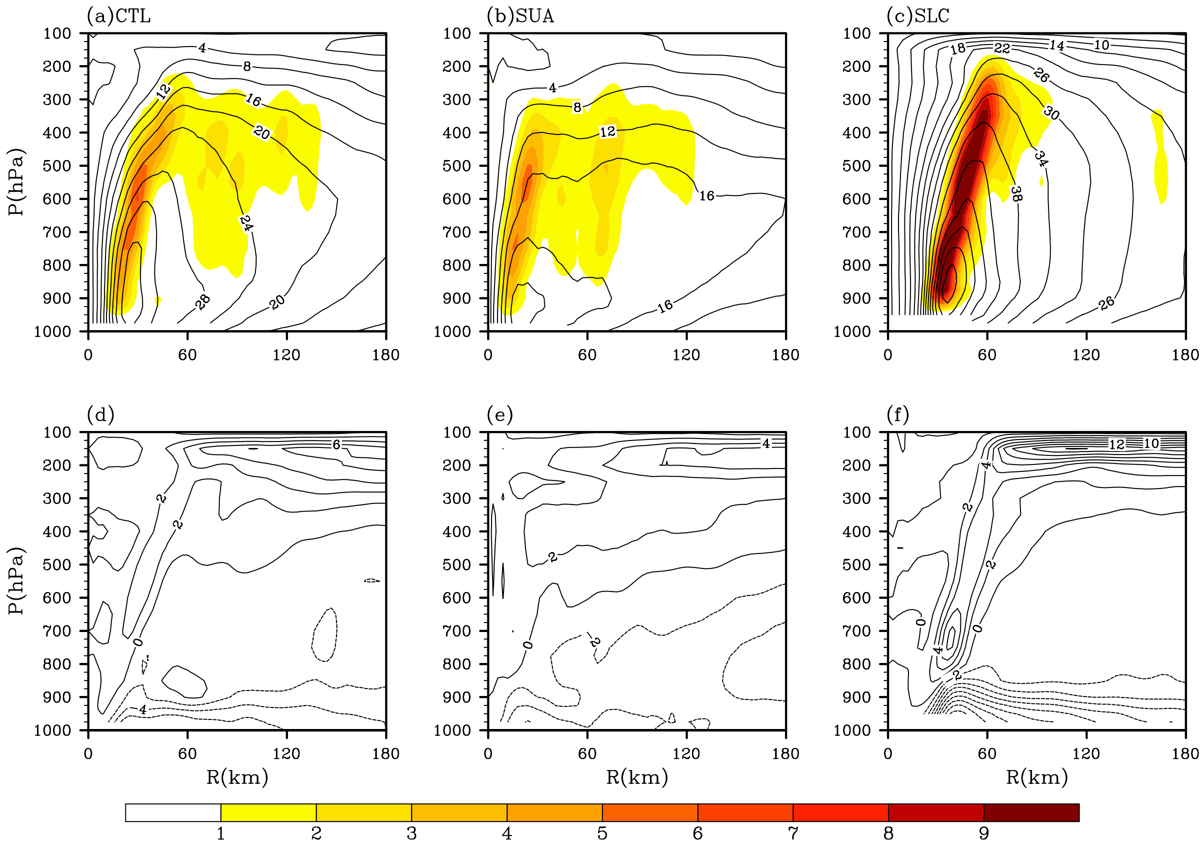

Figure 3. The vertical–radial cross sections of the azimuthal-mean tangential wind (contours, m s^{-1}) and diabatic heating (shaded, 10^{-3} K s^{-1}) in (a) CTL, (b) SUA, and (c) SLC at t = 120 h. (d–f) The same as in Figs. 3a–c except for the radial wind (contours, m s^{-1}).

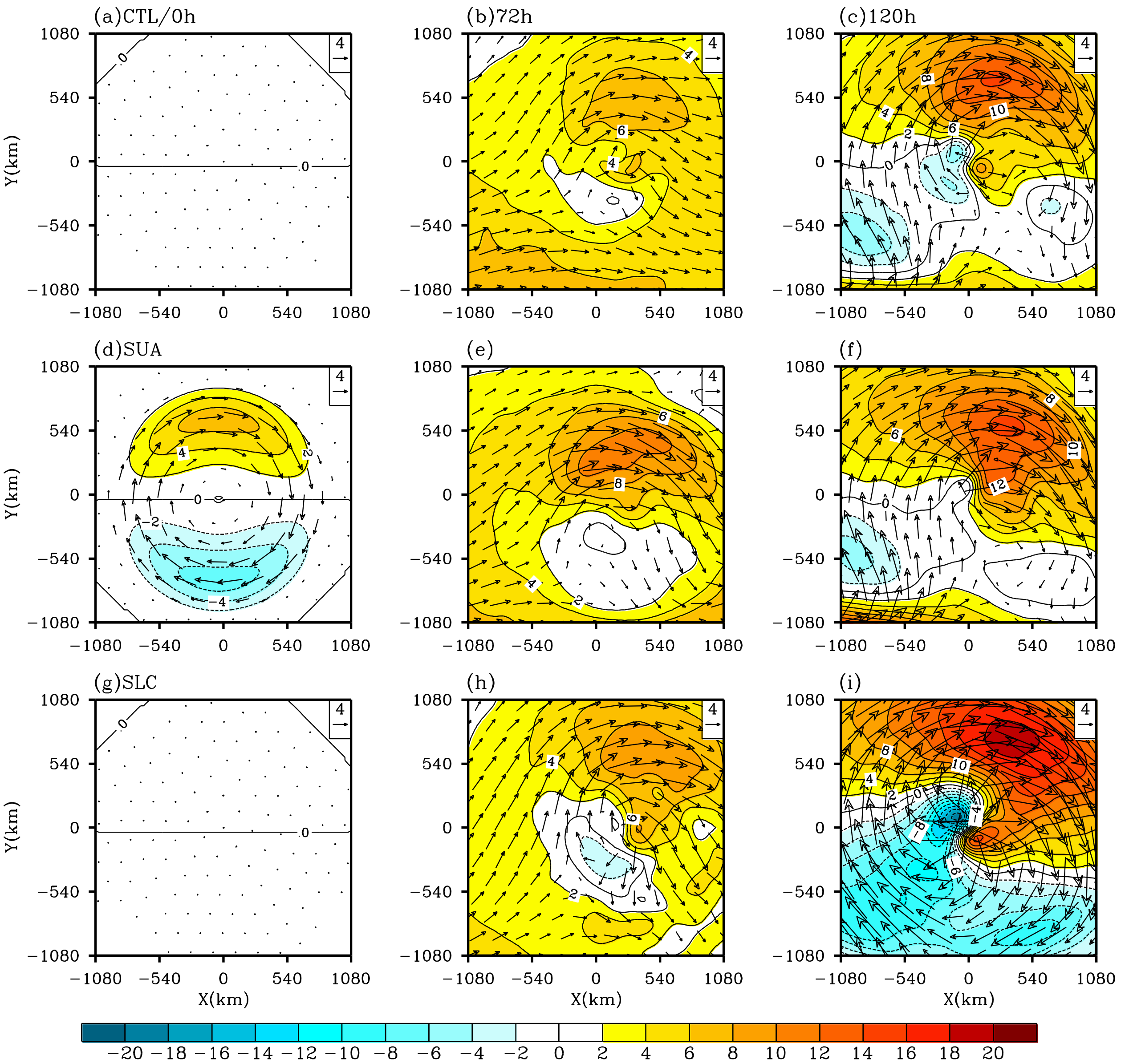

Figure 4. The wind vectors and zonal velocities (shading) at 150 hPa in (a–c) CTL, (d–f) SUA, and (g–i) SLC at t = 0 h (left), 72 h (middle), and 120 h (right) from the 27-km simulation.

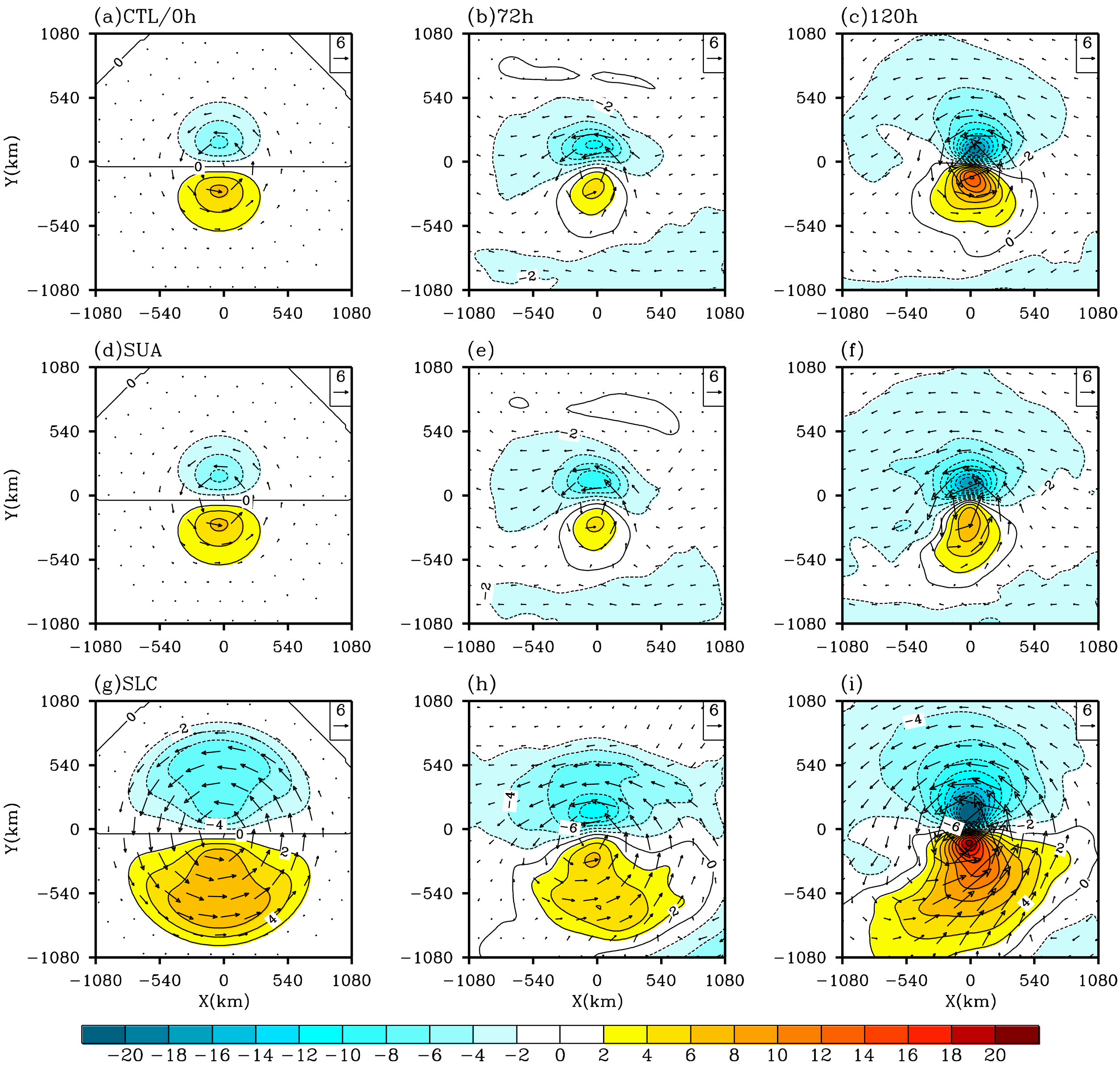

Figure 5. The same as in Fig. 4 but at 850 hPa.

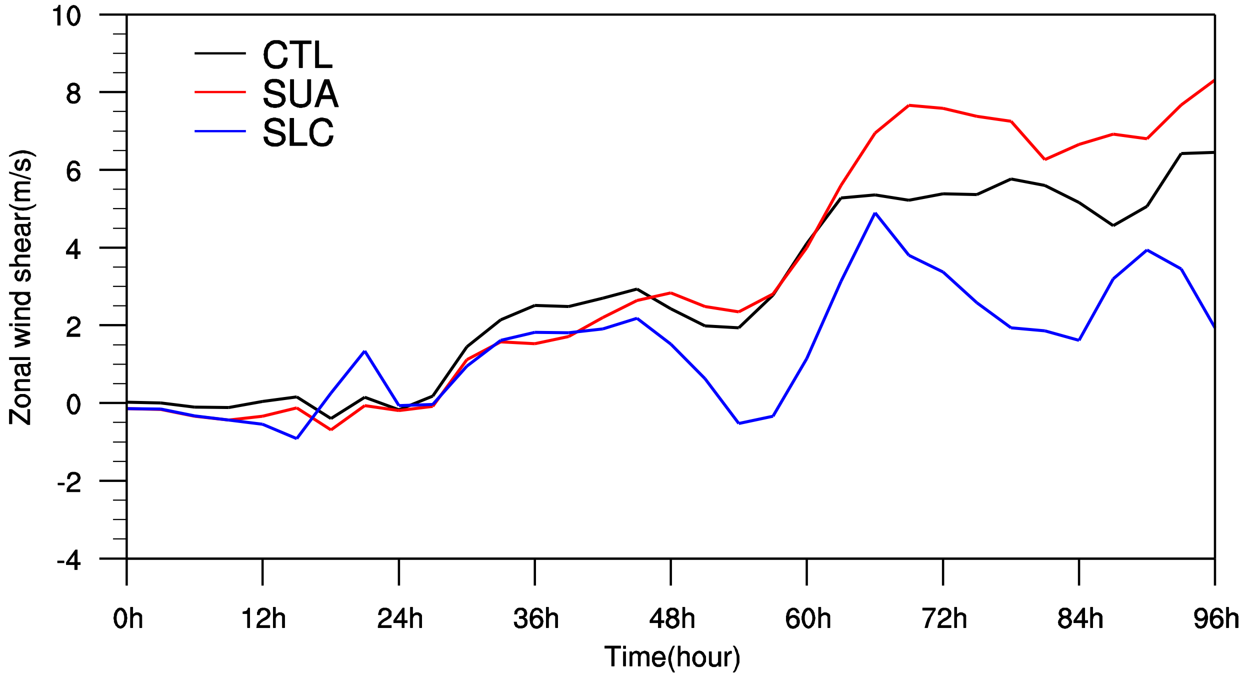

Figure 6. The area-averaged (720 km × 720 km) vertical zonal wind shear (150–850 hPa) of CTL (black), SUA (red), and SLC (blue) from t = 0 h to t = 96 h.

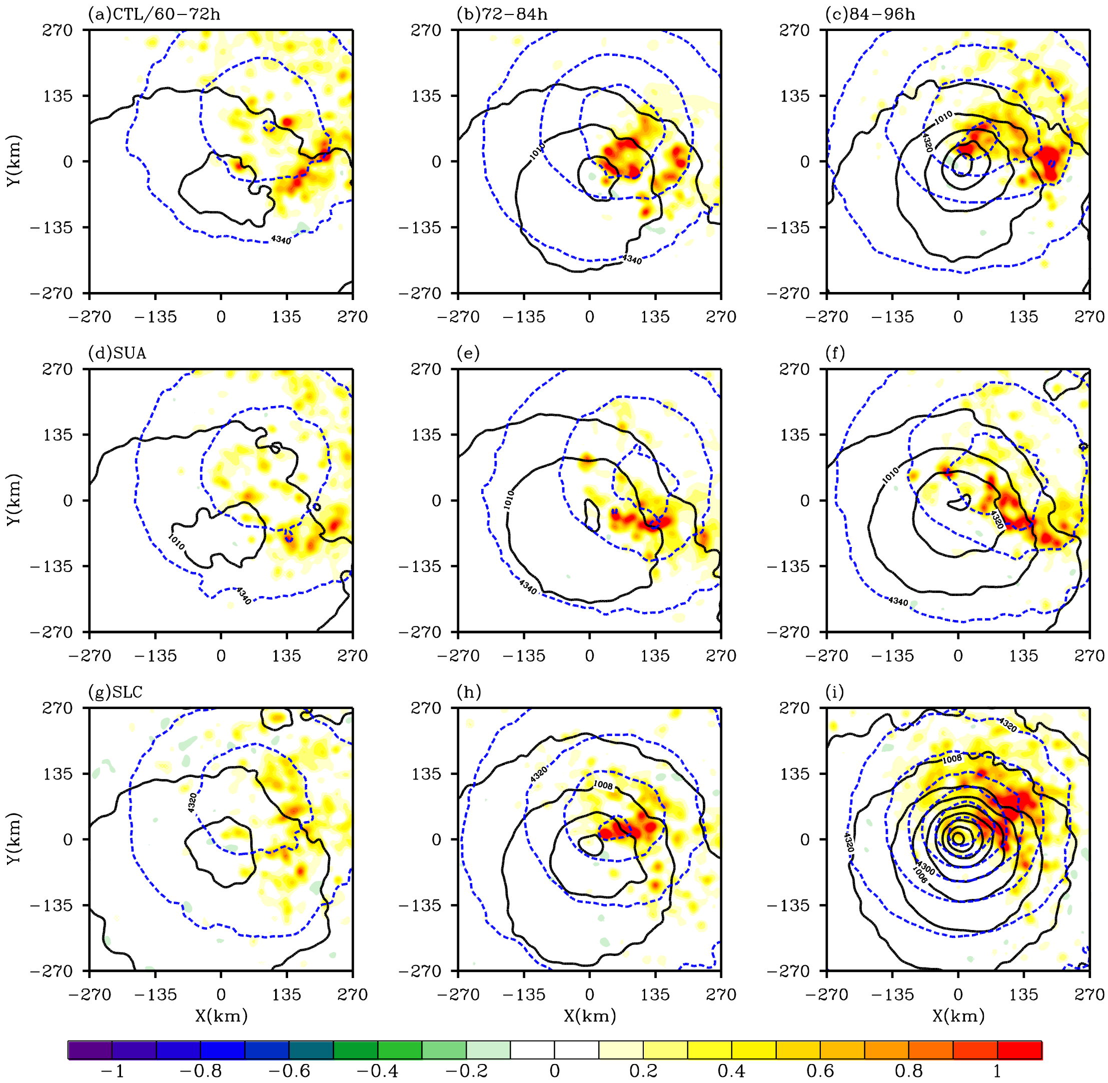

Figure 7. The 600-hPa geopotential height (blue dashed contours), SLP (black solid contours), and 300-hPa vertical velocity fields (shading) in (a–c) CTL, (d–f) SUA, and (g–i) SLC averaged over t = 60–72 h (left), 72–84 h (middle), and 84–96 h (right).

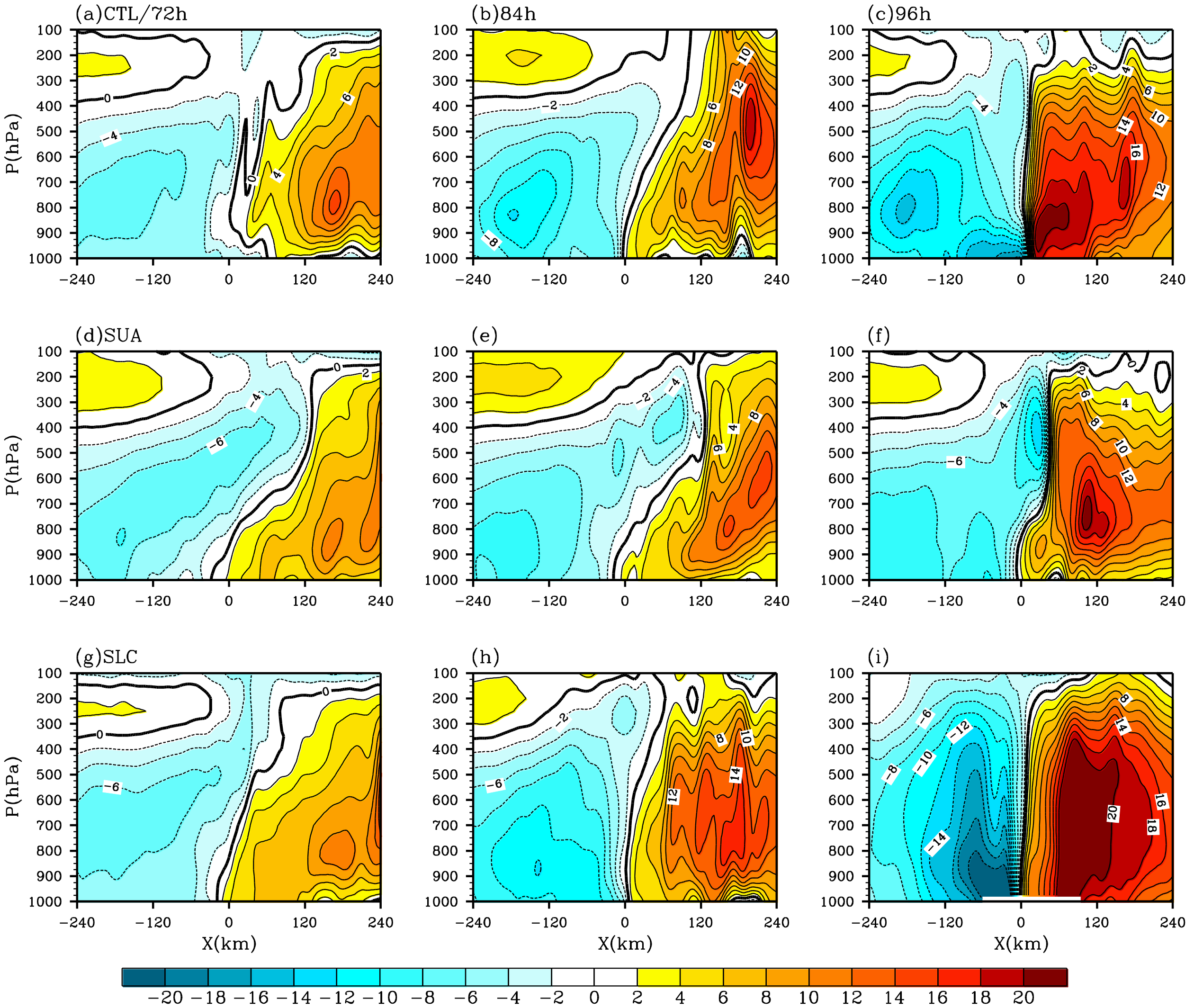

Figure 8. The vertical–zonal cross sections of the meridional wind (m s^{-1}) in (a–c) CTL, (d–f) SUA, and (g–i) SLC at t = 72 h (left), 84 h (middle), and 96 h (right).

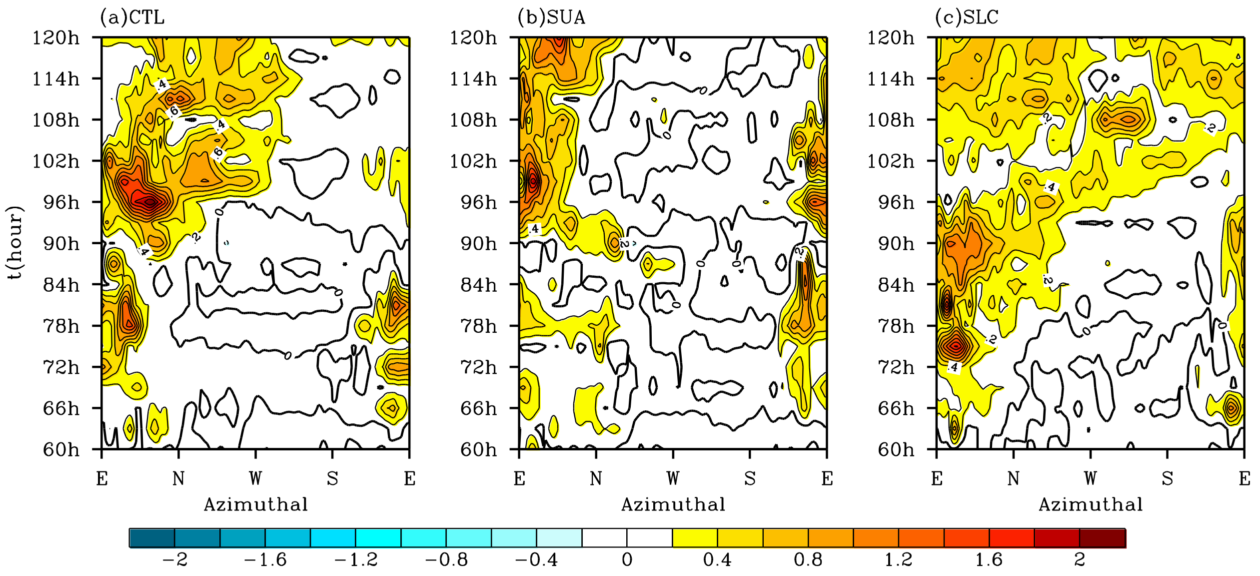

Figure 9. The time-azimuthal cross sections of the radial-mean (0–150 km) vertical motion (m s^{-1}) at 300 hPa for CTL, SUA, and SLC from t = 60 h to t = 120 h.

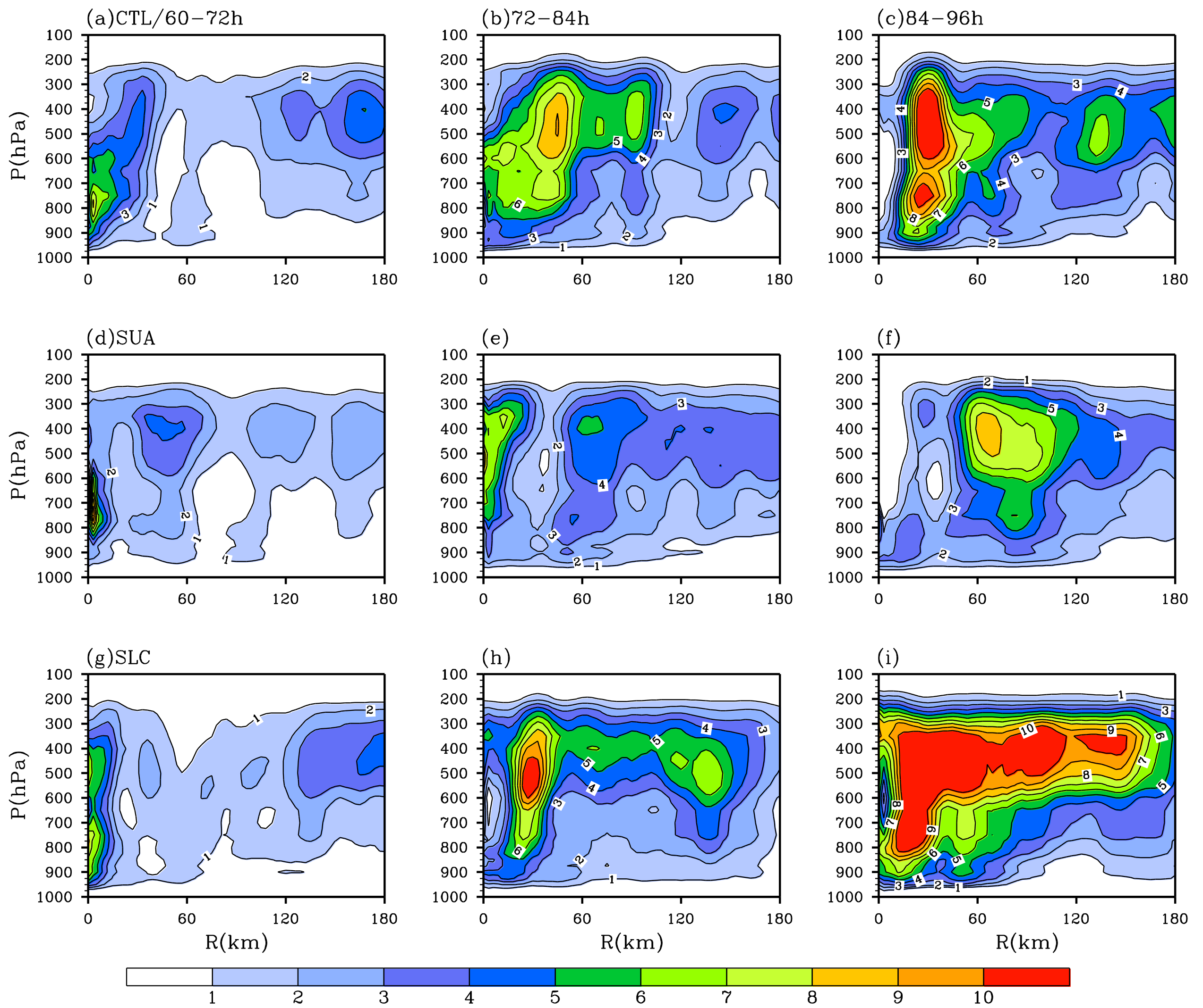

Figure 10. The vertical–radial cross sections of the azimuthal-mean diabatic heating (10^{-4} K s^{-1}) in (a–c) CTL, (d–f) SUA, and (g–i) SLC averaged over 60–72 h (left), 72–84 h (middle), and 84–96 h (right).

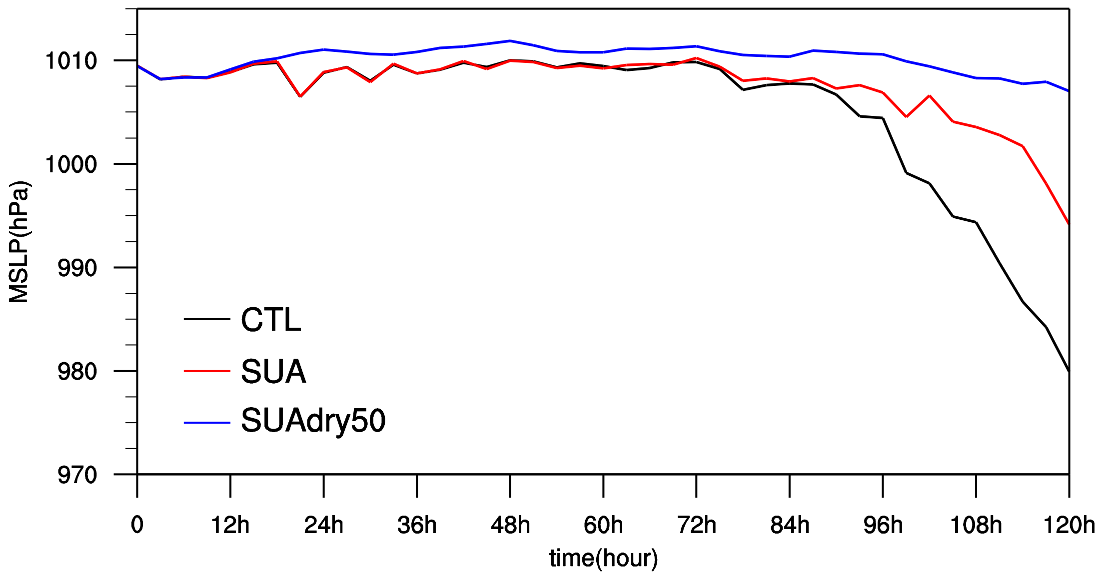

Figure 11. The time evolutions of the MSLP (hPa) in three experiments CTL (black), SUA (red), and SUAdry50 (blue). The abscissa represents time (h) and the ordinate corresponds to the intensity of the MSLP.

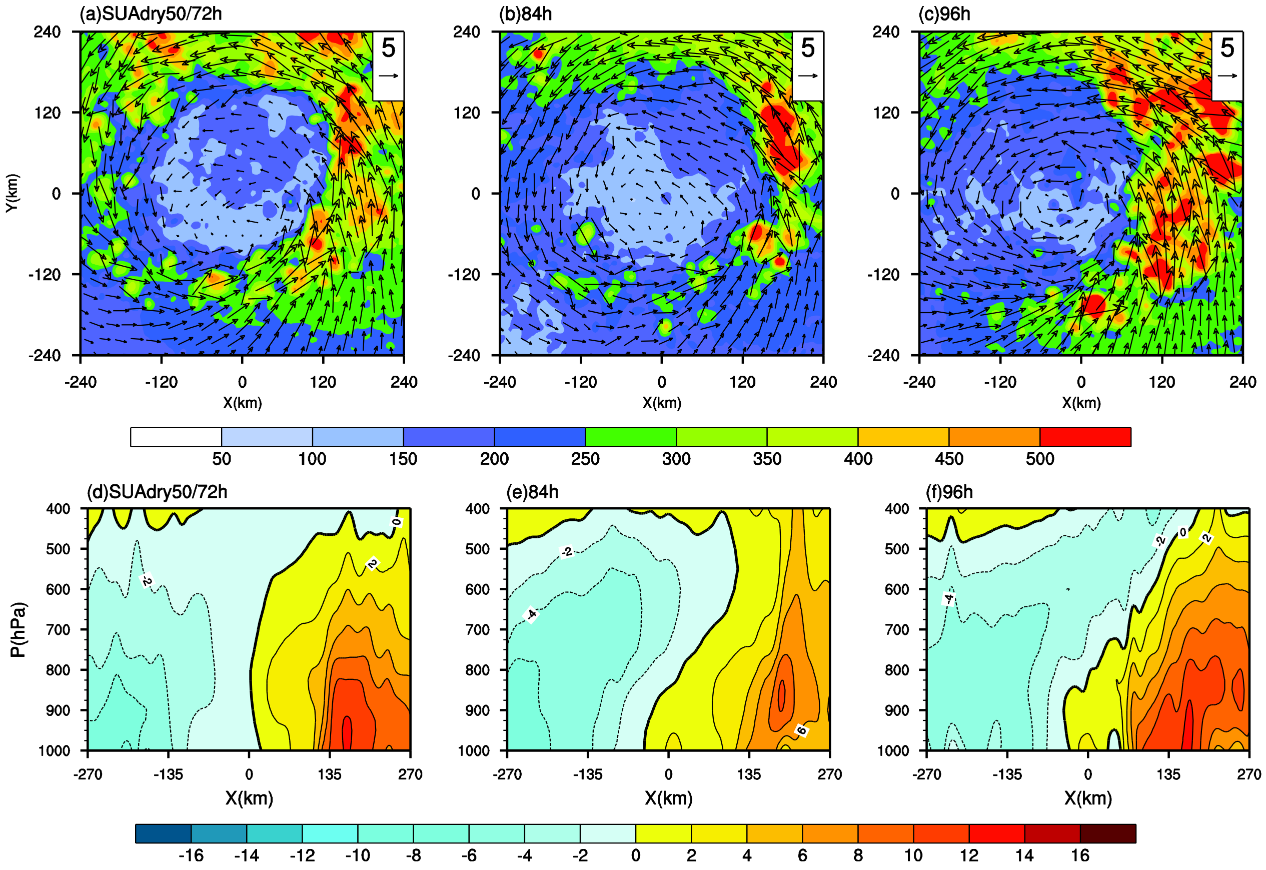

Figure 12. The surface heat fluxes (unit: W m^{-1}) and 10-m winds at (a) t = 72 h, (b) t = 84 h and (c) t = 96 h in SUAdry50. (d-f) The same as in (a-c) except for the vertical–zonal cross sections of the meridional wind (m s^{-1}).

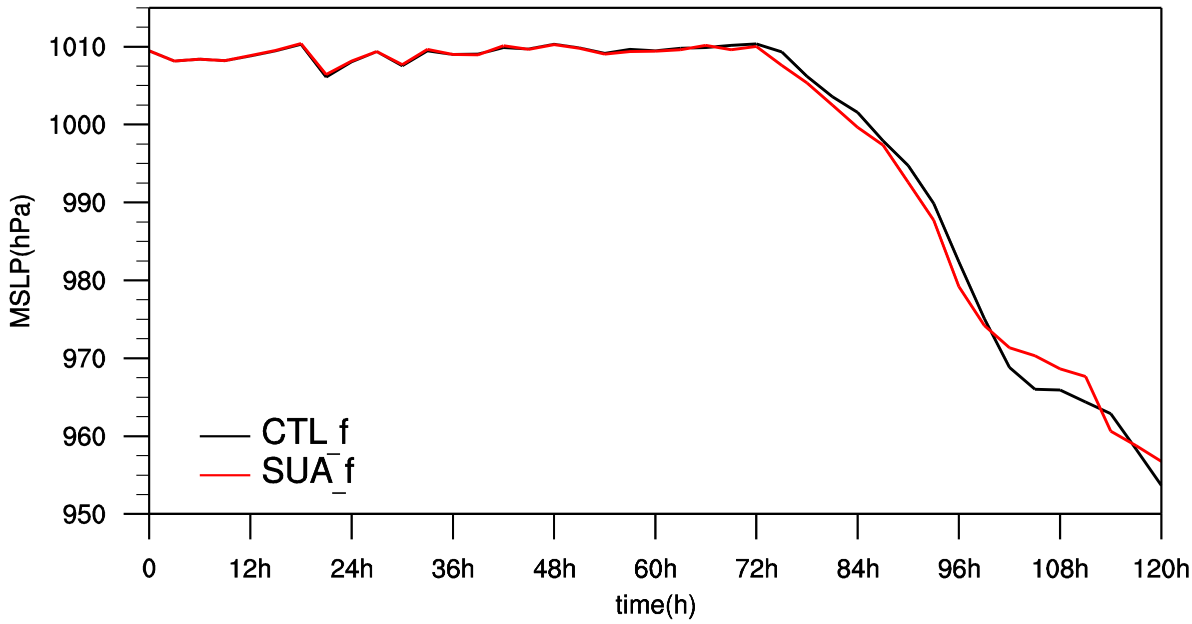

Figure 13. The time evolutions of the MSLP (hPa) in two experiments, CTL_f (black) and SUA_f (red), on an f plane at 15°N. The abscissa represents time (h), and the ordinate corresponds to the intensity.

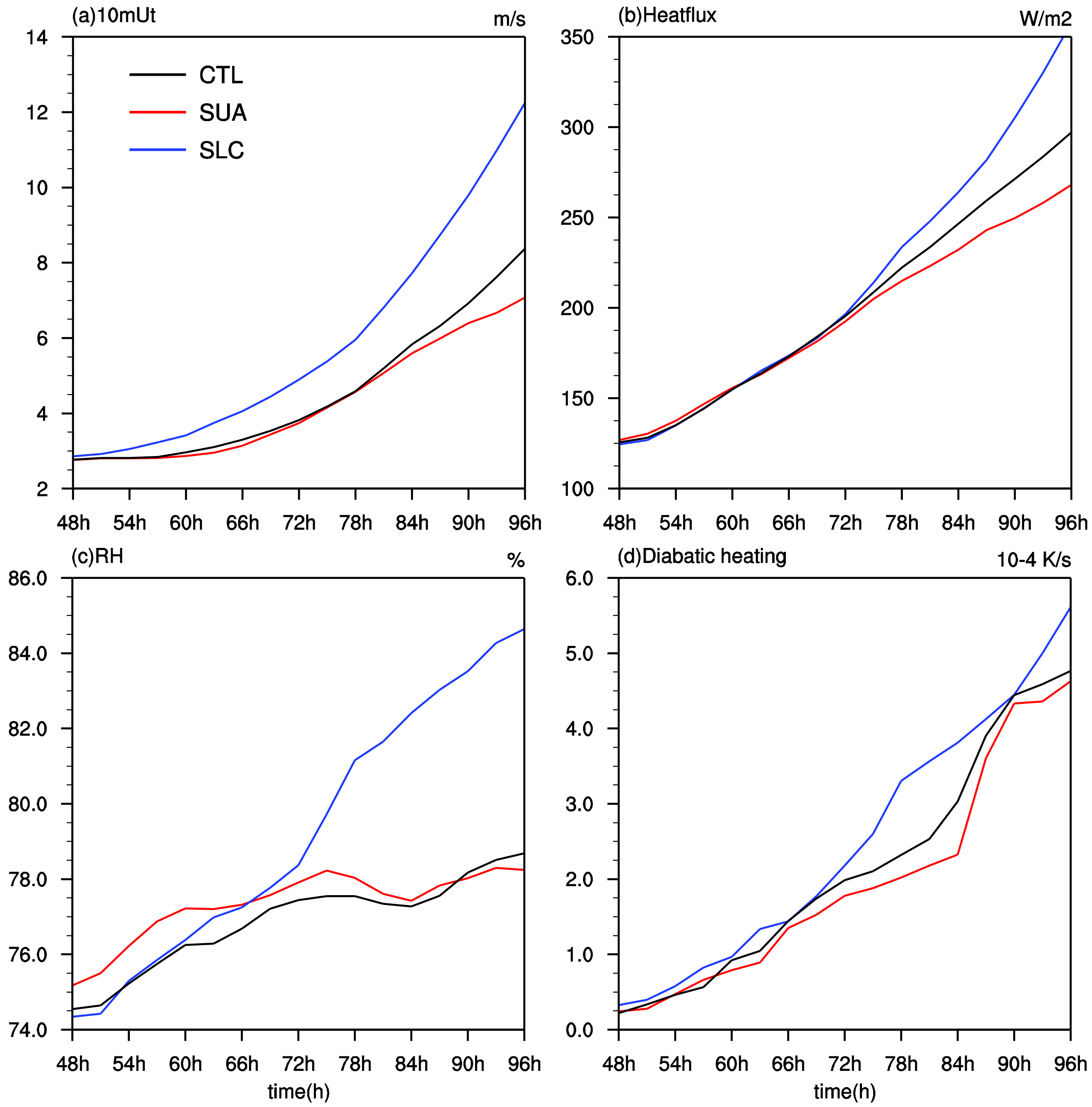

Figure 14. The time evolutions (24-h running mean) of the (a) radial-mean (0-180 km) tangential wind (m s^{-1}) at 10 m, (b) radial-mean (0-360 km) surface heat flux (W m^{-2}), (c) radial-mean (0-180 km) and vertically averaged (1000-300 hPa) relative humidity (%), and (d) vertically averaged (1000-200 hPa) diabatic heating (10^{-4} K s^{-1}) in CTL (black), SUA (red), and SLC (blue) from t = 48 h to t = 96 h.

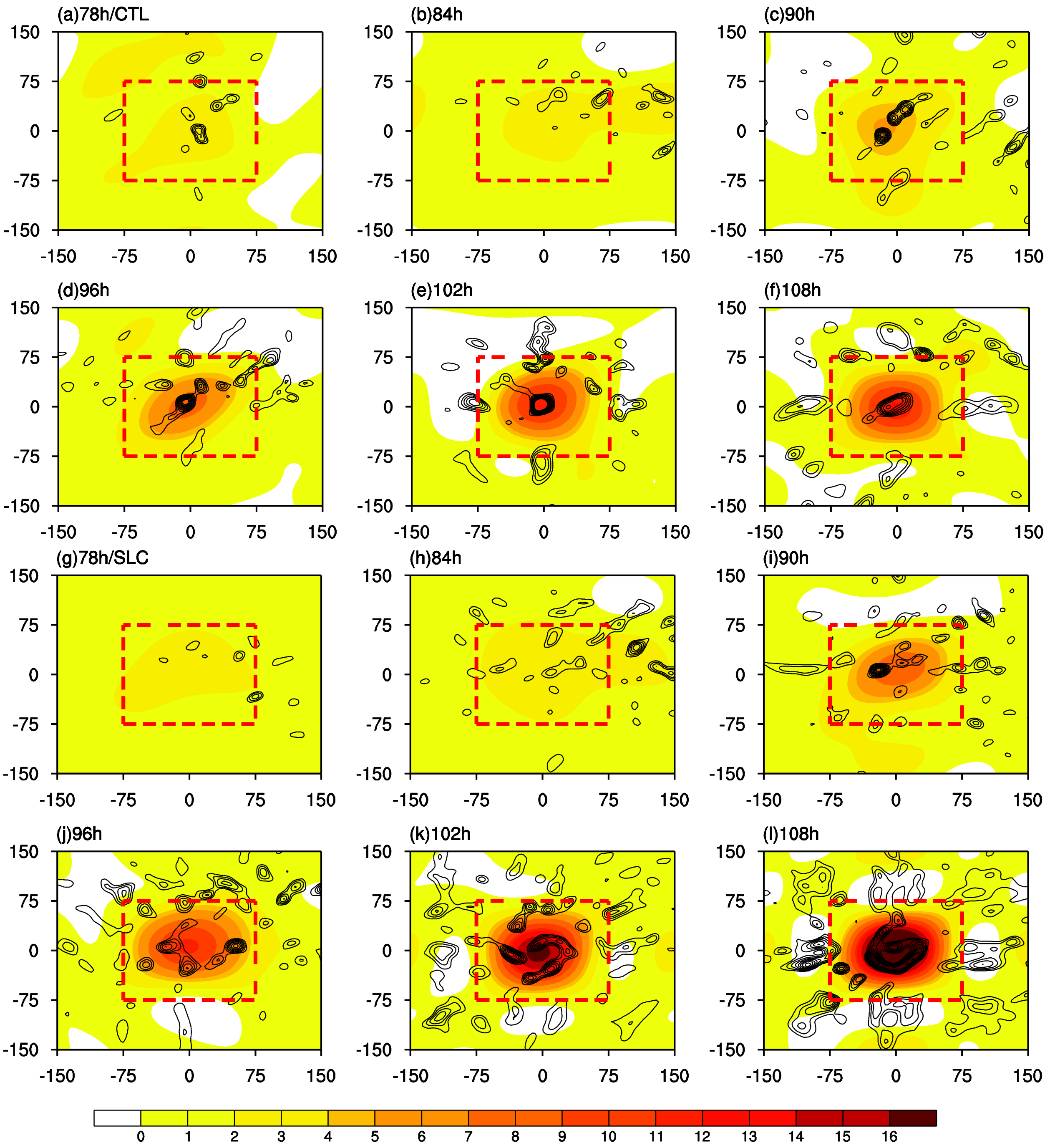

Figure 15. The horizontal distributions of the relative vorticity for the small-scale system (contours, beginning from 3 $\times 10^{-5}$ s^{-1} at an interval of 1 $\times 10^{-5}$ s^{-1}) and the large-scale system (shading, at an interval of 1 $\times 10^{-5}$ s^{-1}) in the (a-f) CTL and (g-l) SLC cases from t = 78 h to t = 108 h at an interval of 6 h. The red box denotes the center region of the vortex.

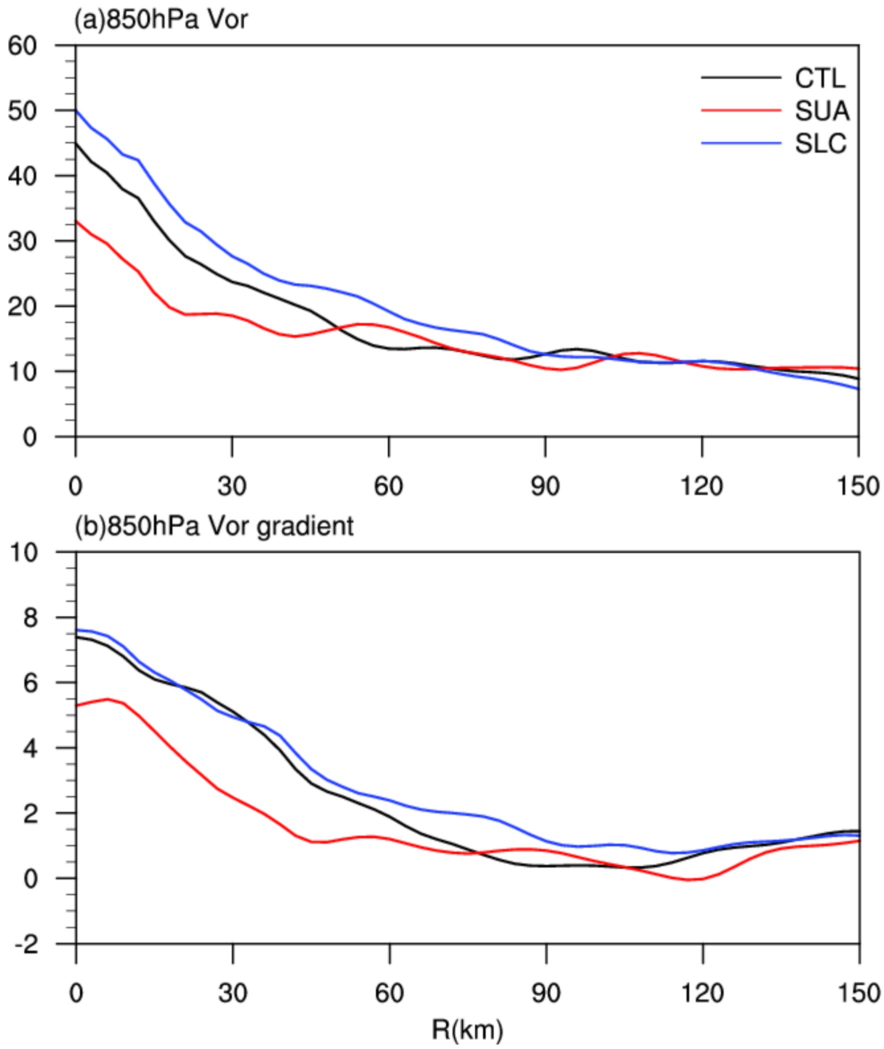

Figure 16. The radial distributions of (a) the relative vorticity (10^{-5} s^{-1}) and (b) the associated 27-km running mean gradient of the relative vorticity (-d(Vor)/dR, 10^{-9} s^{-1} m^{-1}) at 850 hPa in CTL (black), SUA (red), and SLC (blue) averaged from t = 72 h to t = 84 h.

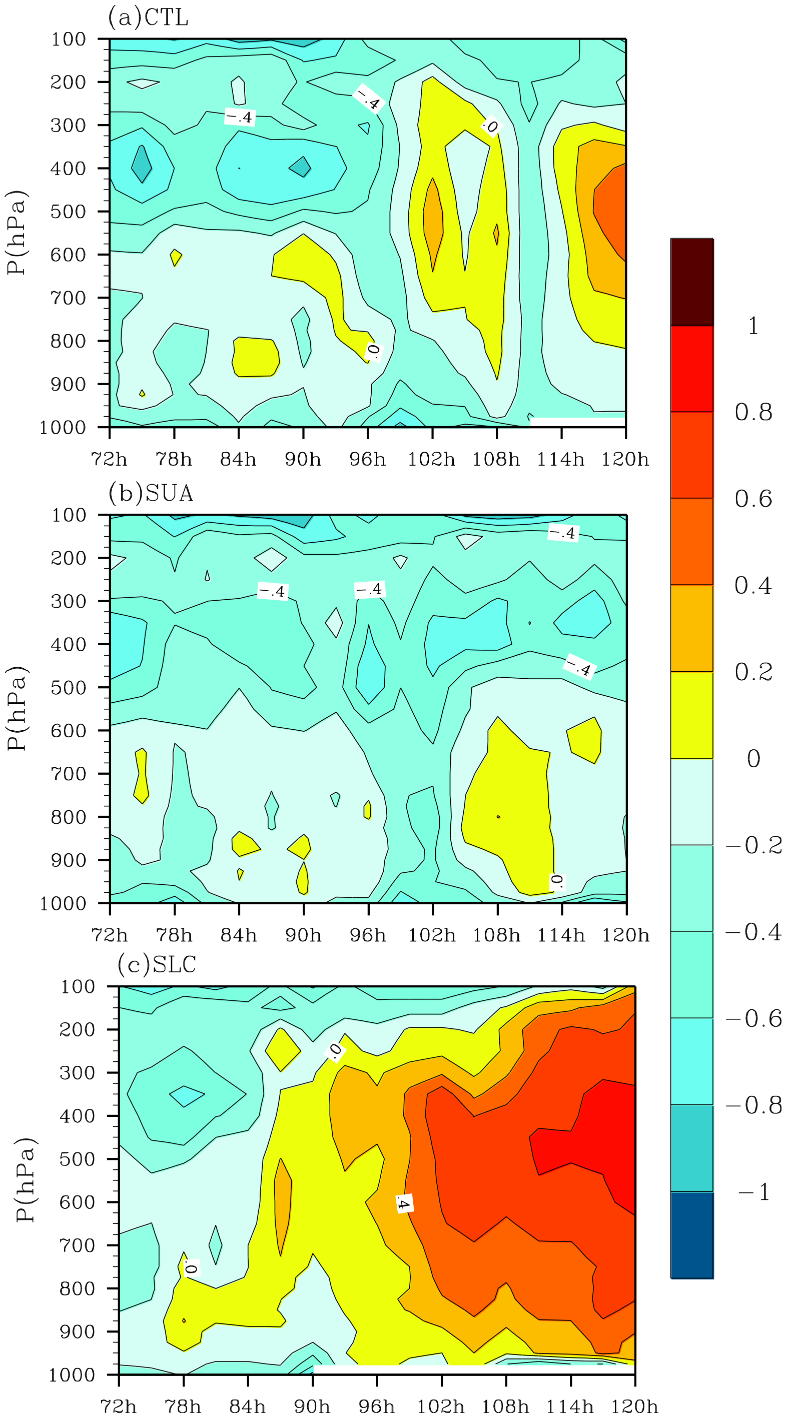

Figure 17. The vertical–time cross sections of the area-averaged OW parameter (60 km × 60 km) from t = 72 h to t = 120 h in (a) CTL, (b) SUA and (c) SLC.

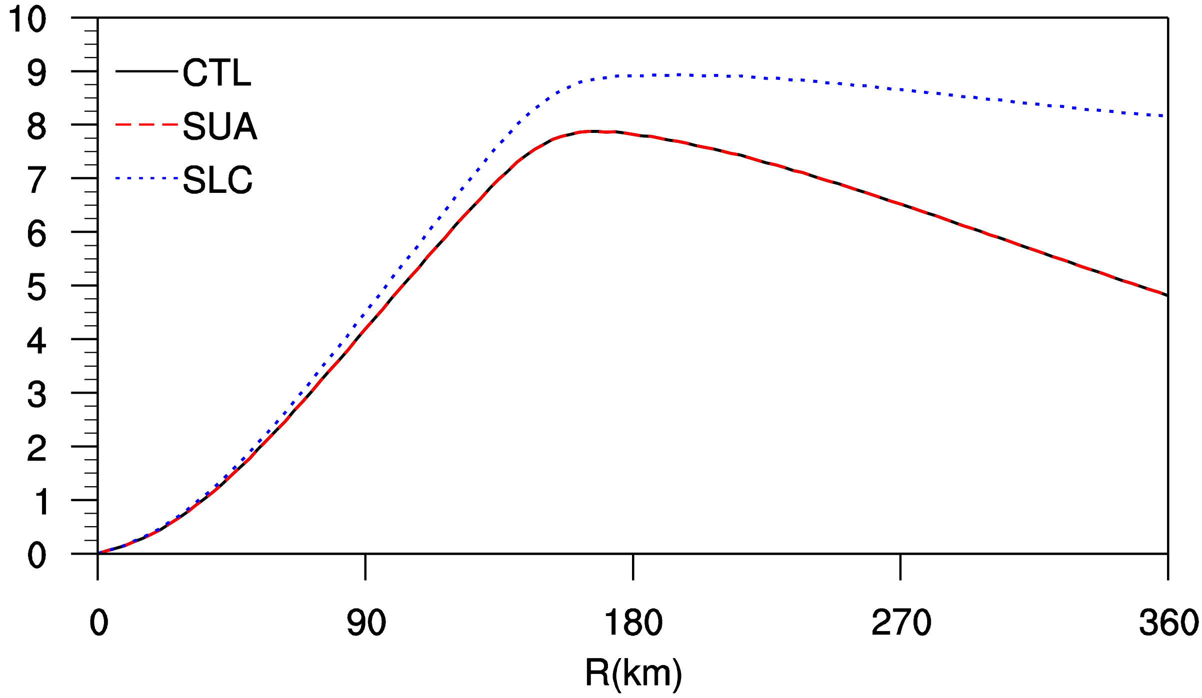

Figure 18. The radial distributions of the azimuthal mean tangential wind of the vortex at the surface (m s^{-1}) in CTL (black), SUA (red), and SLC (blue) at the initial time.

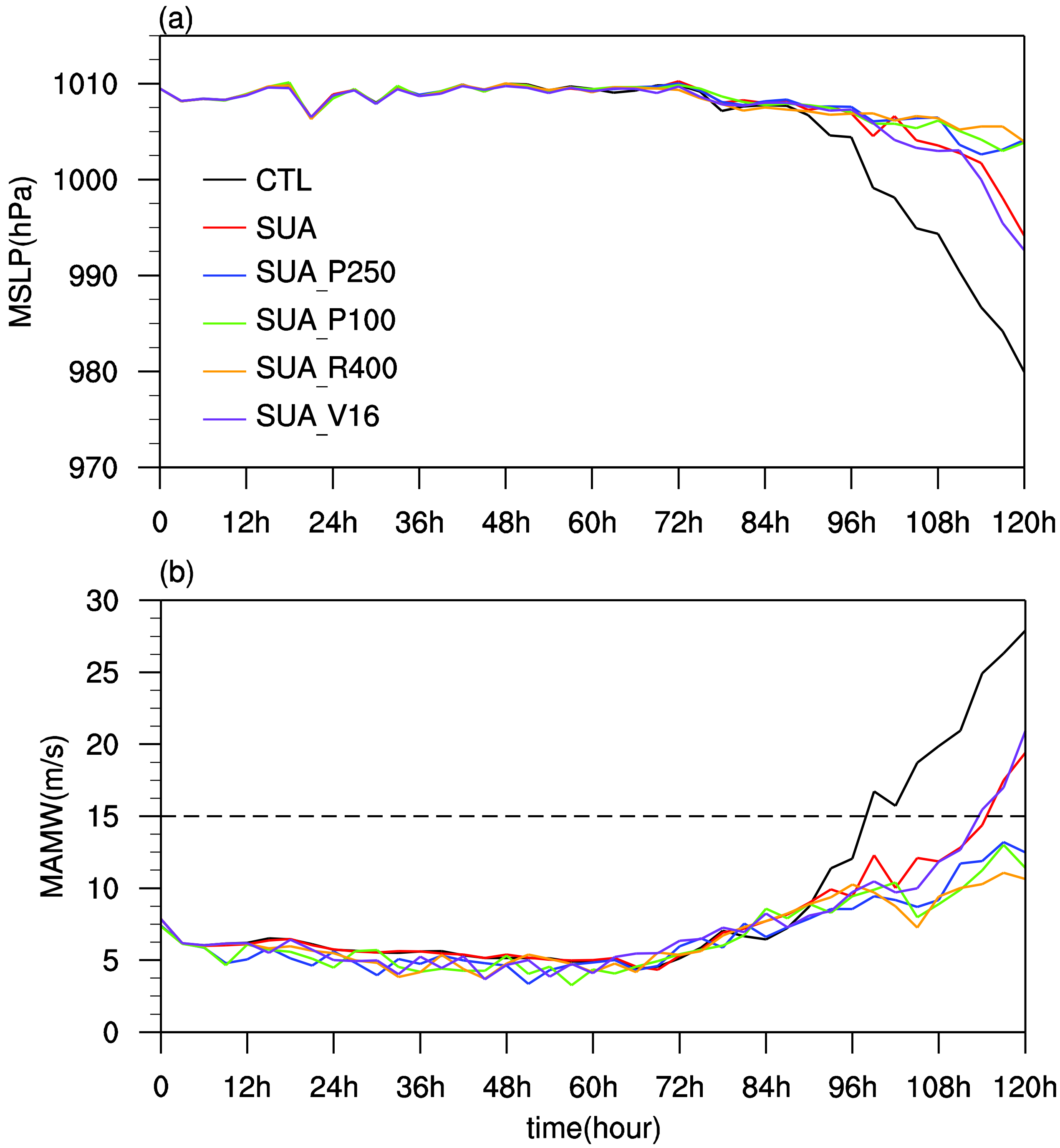

Figure 19. The time evolutions of the (a) MSLP (hPa) and (b) MAMW (m s^{-1}) in CTL (black), SUA (red), SUA_P250 (blue), SUA_P100 (green), SUA_R400 (orange), and SUA_V16 (purple). The abscissa represents the integration time (h), and the ordinate corresponds to the intensity. The dashed line in (b) denotes the TC genesis time when the MAMW speed exceeds 15 m s^{-1}.

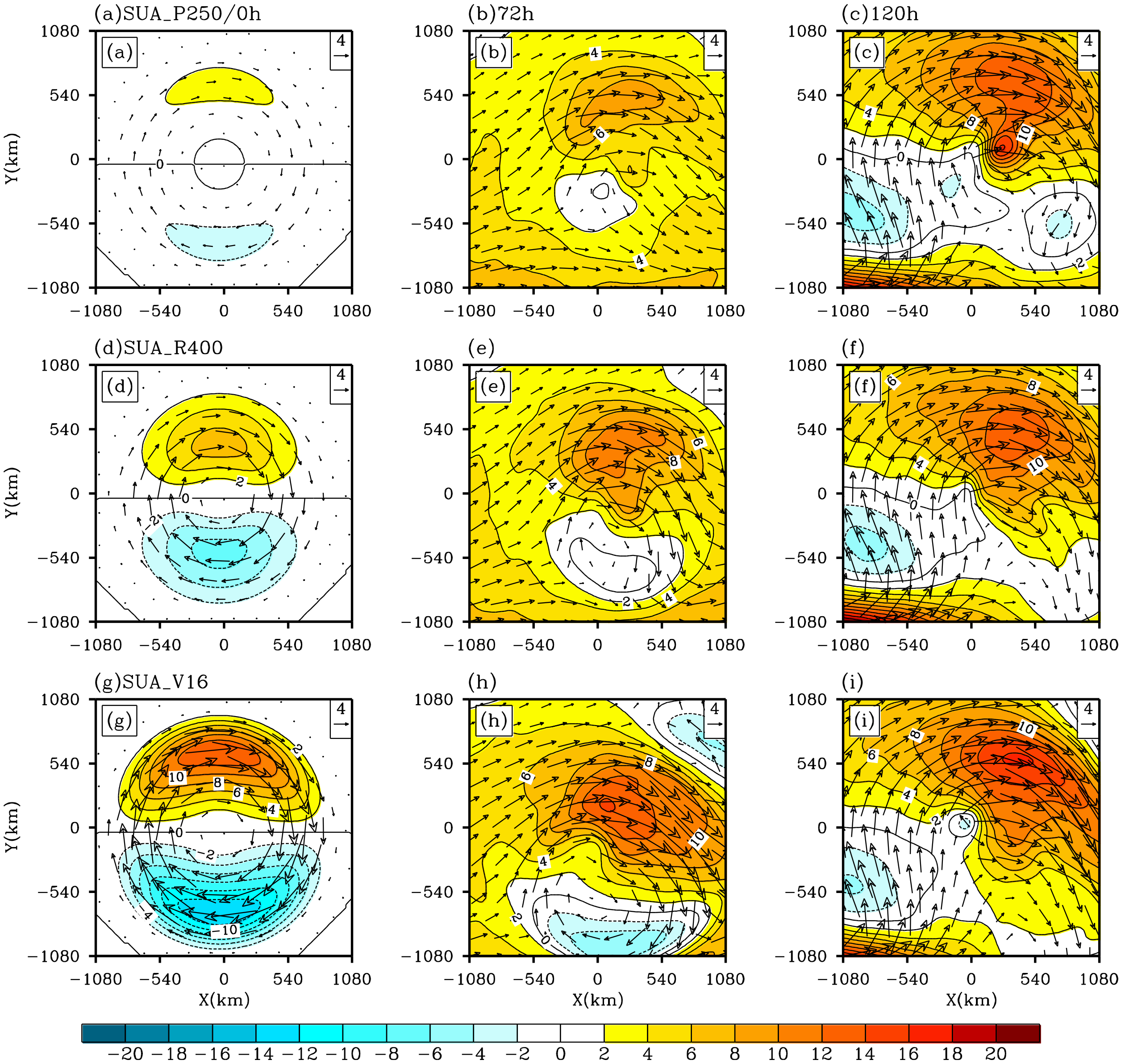

Figure 20. The same as in Fig. 4 but in (a–c) SUA_P250, (d–f) SUA_R400, and (g–i) SUA_V16.

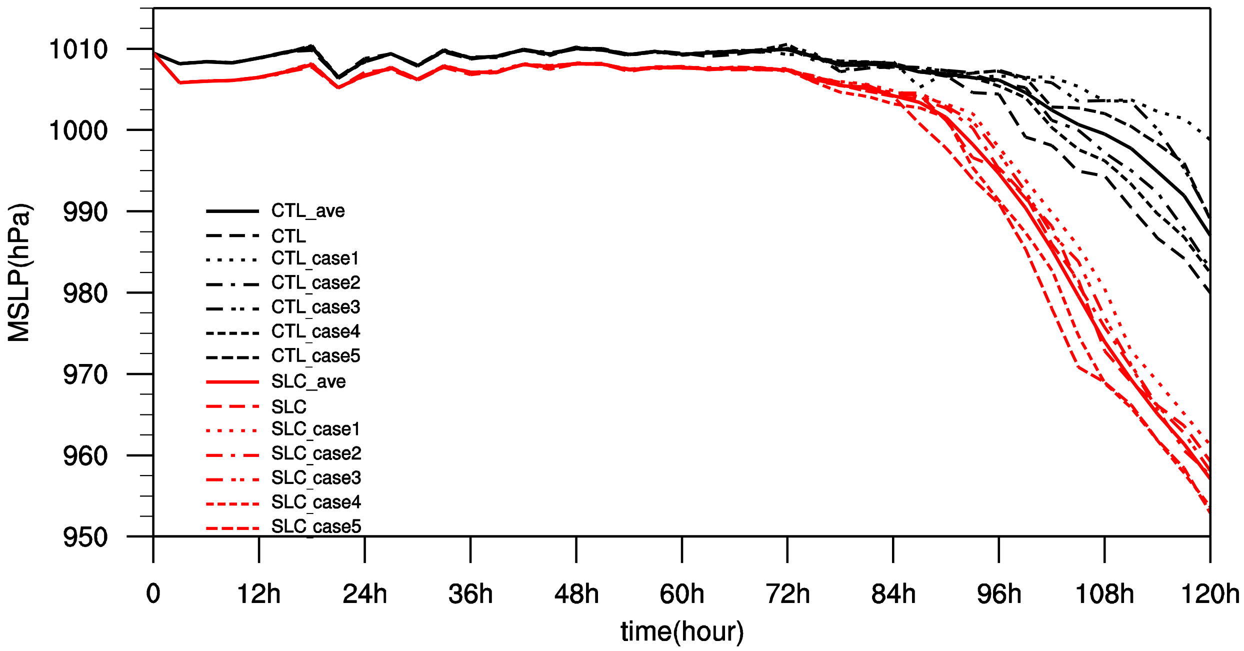

Figure 21. The time evolutions of the MSLP (hPa) in the ensemble experiments of the CTL case (black) and SLC case (red). The abscissa represents time (h), and the ordinate corresponds to the intensity.